ADDITIONAL OBSERVATIONS AND ANALYSIS OF THE LYMAN-α ABSORPTION LINES TOWARD THE QSO PAIR Q0107−025A,B[1,2]

NADINE DINSHAW,[3,4] RAY J. WEYMANN,[5] CHRIS D. IMPEY,[3] CRAIG B. FOLTZ,[6]
SIMON L. MORRIS,[7] AND TOM AKE[8]

ABSTRACT

We present further analysis and discussion of the properties of the absorption lines in the QSO pair Q0107−025A,B (z_{em} = 0.956, 0.952; angular separation 1.29) based upon spectroscopy obtained with the Faint Object Spectrograph (FOS) of the *Hubble Space Telescope* (*HST*). We also present observations of the pair at shorter wavelengths taken with the *HST* Goddard High Resolution Spectrograph low-resolution grating, as well as Multiple Mirror Telescope spectra obtained with the intent of looking for metal-line counterparts to the Lyman-α absorption systems. The most interesting feature revealed by the GHRS spectra is a weak Lyman limit system with a redshift of z_{LLS} = 0.3997. The Lyman limit system itself is seen only in Q0107−025B, but corresponding Lyα lines can be seen in the FOS spectra of both Q0107−025A and B indicating that lower column density gas extends out to greater distances than higher column density gas. From a sample of 5 σ lines with $W_0 > 0.32$ Å detected in the FOS spectra, we count five systems (including a probable system) common to both spectra with velocity differences less than 150 km s^{-1}, and six systems that are not in common to both spectra in the redshift range $0.48 < z < 0.89$. From the presence of common absorption, we obtain lower limits on the radius of the absorbers of 140–160 h^{-1} kpc [$h \equiv H_0/(100$ km s^{-1} Mpc^{-1}); $q_0 = 0.5$]. Using a simple maximum-likelihood analysis, we estimate a characteristic radius of 505 h^{-1} kpc assuming spherical absorbers, with 95% confidence lower and upper limits of $345 < R < 1520$ h^{-1} kpc. For disklike absorbers, we derive a most probable radius of 715 h^{-1} kpc and 95% confidence limits of $470 < R < 2310$ h^{-1} kpc. We also present a new statistical technique to test the relative likelihood of three geometric models. In particular, we consider spherical absorbers, with and without a distribution in size, as well as filamentary and disklike absorbers. Spherical absorbers with uniform radius can be ruled out since they cannot simultaneously reproduce the large equivalent width coincidences and anticoincidences observed. The model that best reproduce the equivalent width distribution of the observed coincident and anticoincident systems corresponds to randomly inclined disks with characteristic radius 915 h^{-1} kpc and 95% confidence interval $560 < R < 1270$ h^{-1} kpc. Our results are in agreement with recent cosmological simulations that produce Lyα forest absorbers in the form of filaments and sheets with coherence lengths as great as 1 Mpc.

Subject headings: galaxies: clusters: general — intergalactic medium — quasars: absorption lines — quasars: individual (Q0107-025A,B)

1. INTRODUCTION

A great deal of progress has been made in understanding the physical properties and evolutionary characteristics of the material producing the Lyα absorption systems seen in QSO spectra. Recent ground-based results from very high-resolution and signal-to-noise echelle spectra indicate significant metal enrichment and clustering on small velocity scales even for high-redshift low column density systems (Cowie et al. 1995; Tytler et al. 1995), but there is no direct evidence on the relationship of these clouds to galaxies. At low redshifts, the data suggest a fairly intimate connection between many intermediate column density Lyα clouds and galaxies (Lanzetta et al. 1995; Le Brun, Bergeron, & Boisse 1996; Bowen, Blades, & Pettini 1996), though a number of low column density clouds have been found in or near voids in the galaxy distribution (Morris et al. 1993; Stocke et al. 1995). Encouraging progress has been made in *N*-body simulations that incorporate gas hydrodynamics (Cen et al. 1994; Zhang, Anninos, & Norman 1995; Hernquist et al. 1996; Miralda-Escudé et al. 1996), and some of the characteristics of the Lyα forest observations are reproduced quite well.

Despite this progress, the actual origin and physical nature of the clouds is far from clear; it is not even clear if the Lyα absorption seen at low redshifts in *HST* spectra represents the same phenomenon as that seen at high redshifts. Critical information for understanding the nature of the Lyα absorption is the geometry and kinematics of the absorbers, which can be constrained by studying two or more lines of sight with small angular separation.

Until fairly recently it appeared that the characteristic transverse sizes of absorbers at redshifts $\gtrsim 2$ were a few tens

of kpc. Recent observations have shown that the characteristic sizes are somewhat larger. In particular, Bechtold et al. (1994) and Dinshaw et al. (1994) find a characteristic radius[9] of order 100 h^{-1} kpc at $z \simeq 2$. Still more recently, Dinshaw et al. (1995; hereafter Paper I) observed lines of sight toward the QSOs Q0107−025A,B ($z_{em} = 0.956$, 0.952; angular separation $1\rlap{.}''29$) and determined for the first time characteristic sizes at much smaller redshifts. The results implied a characteristic radius of at least ~ 150 h^{-1} kpc and perhaps as large as 1 Mpc over the redshift range $0.48 < z < 0.89$.

At face value, these results give a weak indication that the characteristic transverse sizes of the Lyα absorbers may increase with decreasing redshift, and there is growing evidence from *HST* observations of paired lines of sight at redshifts $1.06 < z < 1.69$ that the evolution in the cloud radius may be real (Dinshaw et al. 1998). However, Fang et al. (1996) have suggested that the more significant correlation is one between inferred cloud size and line-of-sight separation, which they attribute to a distribution in cloud size.

It is not yet clear if the majority of the Lyα absorbers at redshifts $z \lesssim 1$ arise from the same mechanisms that produce the high-redshift absorbers. Study of the relation of the distribution of the absorbing material along more than one line of sight with galaxies may give us some clues about the topology and kinematic structure of the absorbers. We are currently surveying the neighboring galaxies in the field of Q0107−025A,B in order to study the spatial correlation between the galaxies and the Lyα absorbers seen in *HST* GHRS spectra of the pair. The results will be presented in a forthcoming paper.

The remainder of the paper is organized as follows: In § 2, we present spectroscopic observations of Q0107−025A,B and describe the procedure used to select significant absorption lines in the spectra. In § 3, we describe in detail the method used to identify the lines. In § 4, we define two complete samples of Lyα absorption lines that we use to determine the size of the absorbers, and we also discuss the properties of the observed Lyman limit and metal-line systems. In § 5, we apply a maximum-likelihood technique to estimate the characteristic size of the Lyα absorbers. In the same section, we develop a new likelihood method to explore different absorber geometries. Finally, in § 6, we summarize and discuss our results. Throughout this paper, we assume a cosmological model with $H_0 = 100$ km s^{-1} Mpc^{-1} and $q_0 = 0.5$, except where explicitly stated, and we

---

[9] The meaning of the "characteristic radius" is somewhat imprecise. In the present context it refers to the most likely impact parameter for an assembly of assumed identical spherical clouds that yield Lyα absorption above some equivalent width threshold—typically ~ 0.3 Å.

TABLE 1
PROGRAM QSOS

QSO	R. A. (J2000)	Decl. (J2000)	g	z_{em}
Q0107−025A......	01 10 13.16	−02 19 54.3	17.9	0.956
Q0107−025B......	01 10 16.27	−02 18 52.2	17.3	0.952

NOTE.—Units of right ascension are hours, minutes, and seconds, and units of declination are degrees, arcminutes, and arcseconds.

express the dependence upon the Hubble constant by means of the parameter $h \equiv H_0/(100$ km s^{-1} Mpc$^{-1})$.

2. DATA

In this section, we present observations of the Lyα forest obtained with the FOS and GHRS on the *HST*, as well as ground-based data taken with the Multiple Mirror Telescope in order to search for metal systems associated with the Lyα absorption lines. The program QSOs are listed in Table 1, along with their J2000 coordinates, Gunn g magnitudes, and redshifts. The coordinates were measured by the support staff at the Space Telescope Science Institute (STScI) using the Guide Star Selection System Astrometric Support Package (GASP), and are accurate to $1''$. The improved coordinates give an angular separation of the lines of sight of $1\rlap{.}''29$. Magnitudes and redshifts are from Surdej et al. (1986). A journal of all the observations presented in this paper is given in Table 2.

2.1. *The FOS Spectra*
2.1.1. *Observations and Data Reduction*

A preliminary account of the FOS observations was reported in Paper I. A more detailed description of the observations is provided here. We obtained ultraviolet (UV) observations of Q0107−025A,B on 1994 February 12 UT with the post-COSTAR Faint Object Spectrograph (FOS) on *HST*, using the red Digicon detector, $1''$ circular aperture, and G190H grating. This configuration yields a spectral resolution (FWHM) of 1.4 Å, or 200 km s^{-1}, over the wavelength range from 1625–2300 Å. The spectra were obtained in ~ 20 minute exposures with a total of 222 minutes accumulated on Q0107−025A and 108 minutes on Q0107−025B. The signal-to-noise ratio (SNR) in the spectrum of Q0107−025A is at least 12 per pixel in the continuum shortward of ~ 2000 Å and approaches 25 per pixel at longer wavelengths. The SNR for Q0107−025B is slightly poorer: 10 and 22 per pixel shortward and longward, respectively, of ~ 2000 Å.

The FOS spectra were reduced at the STScI via the STSDAS pipeline processing facility in IRAF. Post-COSTAR "superflats" (Lindler et al. 1993) and inverse

---

TABLE 2
JOURNAL OF SPECTROSCOPIC OBSERVATIONS

QSO	Date	Telescope	Instrument	Grating	Exposure (s)	Wavelength (Å)	Resolution (Å)
Q0107−025A......	1994 Feb 12	*HST*	FOS	G190H	13320	1625–2300	1.4
	1994 Nov 15	*HST*	GHRS	G140L	9792	1220–1495	1.4
	1994 Sep 29	MMT	Blue Channel	832 gpm	6600	4150–5650	1.0
	1994 Oct 02	MMT	Blue Channel	832 gpm	9600	3250–4250	1.0
Q0107−025B......	1994 Feb 12	*HST*	FOS	G190H	6480	1625–2300	1.4
	1994 Sep 22	*HST*	GHRS	G140L	9792	1220–1495	1.4
	1994 Sep 29	MMT	Blue Channel	832 gpm	4800	4150–5650	1.0
	1994 Oct 02	MMT	Blue Channel	832 gpm	5400	3250–4250	1.0

sensitivity files were used to flat field and flux calibrate the data, respectively. A correction was also performed for dead and disabled diodes using the reference file recommended for data obtained after 1993 September 13.

A potentially significant source of uncertainty in the zero point of the wavelength scale is caused by nonrepeatability in the positioning of the filter-grating wheel. This error can be unacceptably large, amounting to 0.35 diodes, if calibration exposures are not obtained at the same time as the target exposure (FOS Instrument Handbook, Version 6.0, 1995 June). Given the need for accurate measurements of the zero-point shift between the two spectra and the fact that only one Galactic absorption line falls within the wavelength range of the G190H grating, the acquisition of calibration exposures was important for this program. We obtained one exposure of a PtCrNe comparison lamp for each target and required that the filter-grating wheel not be moved between target exposures. The wavelengths were then recalibrated using the lamp exposures. The rms errors in the wavelength coefficients were no more than ~0.06 Å or 9 km s^{-1}.

By far, the dominant remaining uncertainty in the wavelength zero point is due to *HST* pointing errors that arise from the relative placement of the two QSO images in the 1″ aperture of the FOS. Since the same guide star was used during the exposures of both QSOs, this radial error is expected to be about 0.12″ (1 σ; private communication with FOS Instrument Team), yielding an error projected along the dispersion direction of up to 0.28 Å or 42 km s^{-1}. This effect is systematic in the sense that it shifts all of the

lines in one spectrum relative to those in the other. The observed wavelengths of the only Galactic line accessible with the G190H grating (Al II λ 1671) indicate a relative shift between the spectra of Q0107−025A and B of 20 ± 36 km s^{-1}, well within the estimated uncertainty from pointing errors. Therefore, we do not believe there is a large systematic shift between the spectra, and we made no attempt to correct for a zero-point shift in the wavelengths since the Galactic Al II λ 1671 lines in both Q0107−025A and B appear to be contaminated by the Lyγ lines associated with the common redshift system at $z_{abs} \simeq 0.719$.

Figures 1 and 2 show the flux calibrated spectra and their 1 σ error arrays derived from photon statistics. The broad emission lines at 2020 Å are blends of O VI λλ1031,1037, with possibly some contribution from Lyβ. The emission feature in Q0107−025A shows a double-peaked structure, where the peaks correspond well in redshift to the O VI doublet. This is the first case we are aware of where the blend of O VI λ1031 and O VI λ1037 in emission appears resolved. The continuum fits and significant lines are also shown in the figures. We describe the procedure used to fit the continuum and select significant lines in the next section.

2.1.2. *Continuum Fitting and Selection of Significant Absorption Lines*

An interactive program written by T. Aldcroft (Aldcroft 1993) was used to fit the continua shown in Figures 1 and 2. The program iteratively fits cubic splines to the average of a specified number of data points, where the tightness of the
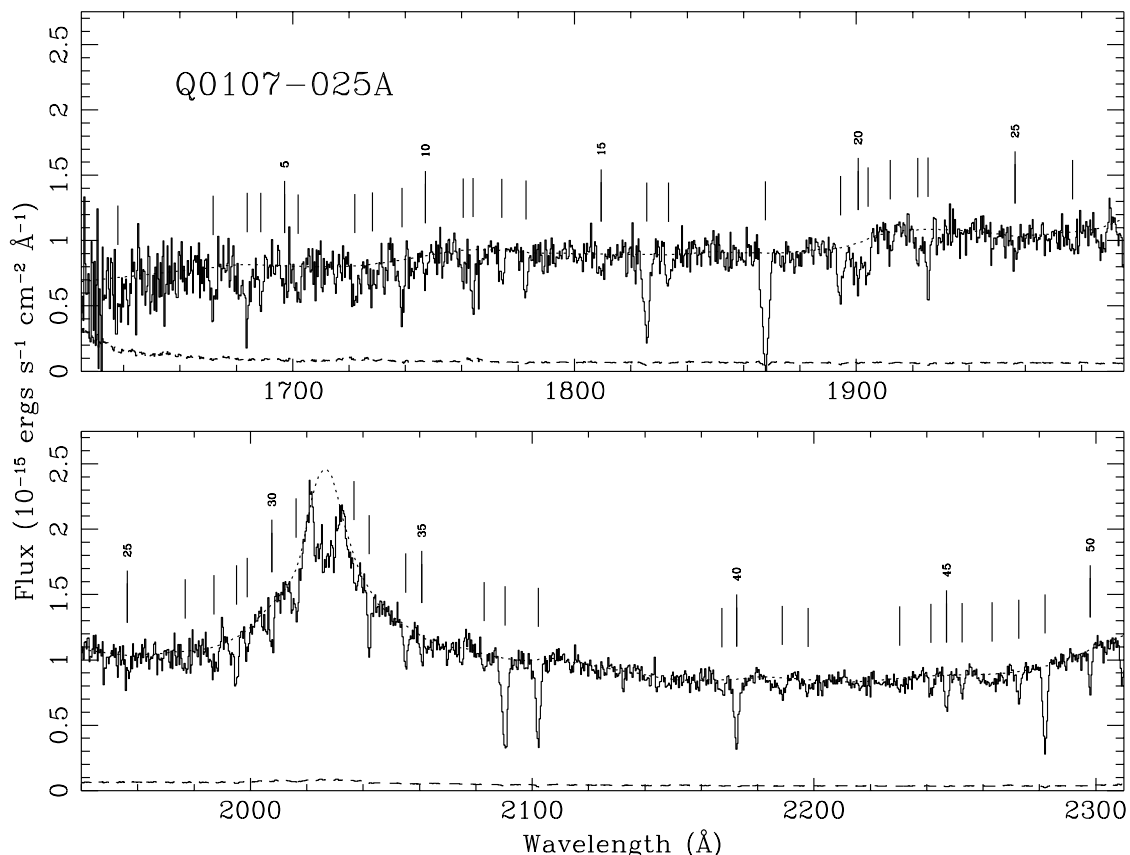

FIG. 1.—Spectrum of Q0107−025A obtained with the *HST* FOS as a function of vacuum wavelength. The dashed line shows the 1 σ error in the flux. The dotted line represents the continuum fit. Tick marks indicate absorption features detected at or above the 3.5 σ confidence level. The emission feature near 2020 Å is a blend of O VI λλ1031,1037, with possibly some contribution from Lyβ.
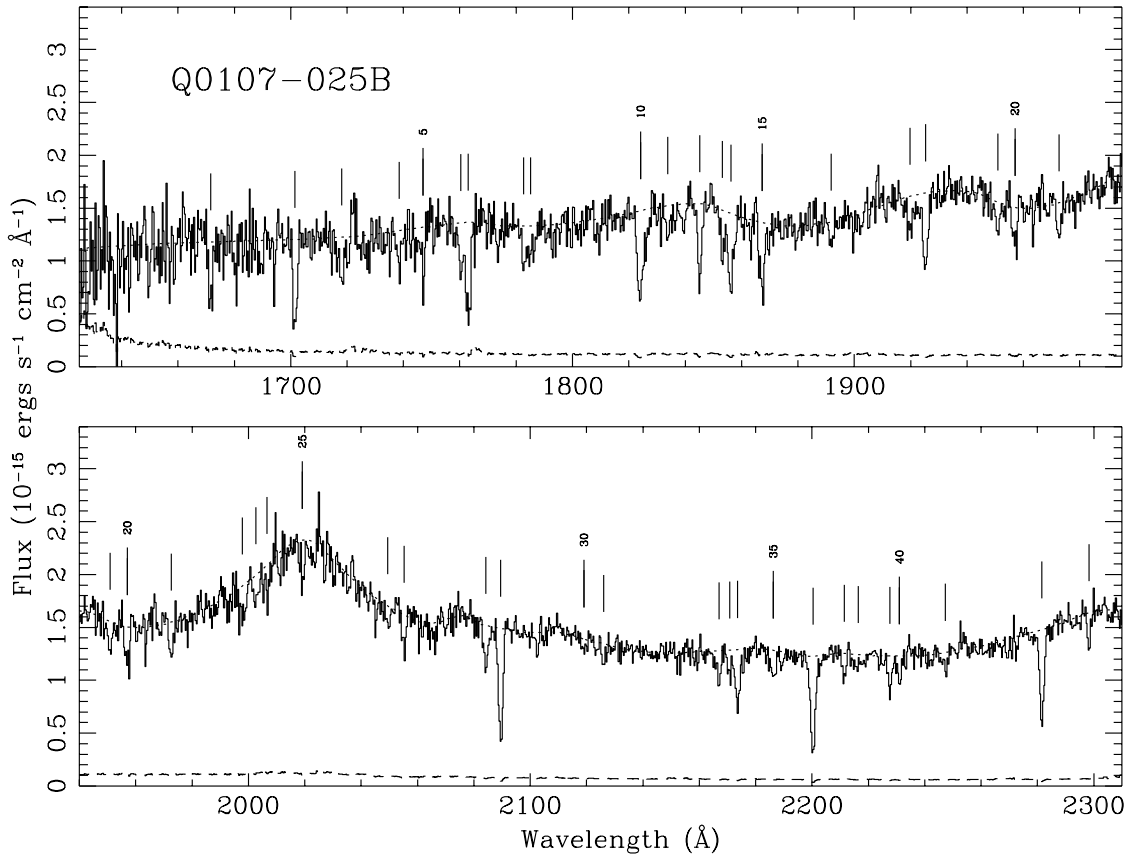
FIG. 2.—Same as Fig. 1, for Q0107−025B

fit is determined by the number of points used in the average. Points deviating negatively by more than 2 standard deviations from the estimated continuum are rejected from subsequent iterations until the rms positive and negative residuals in the remaining points are equal. The fit typically converged in less than four iterations. In order to establish whether the undulations in the spectra of Q0107−025A,B are artifacts or weak emission features, we compared our data with the composite of five *HST* FOS spectra taken with the G160L grating (Hamann, Zuo, & Tytler 1995). By adjusting the continuum level to compensate for differences in the equivalent width and slope, the composite spectrum looked remarkably like those of Q0107−025A and B. The agreement, however, was not sufficient to use the composite as the true continuum, but was useful in guiding the placement of the continuum fits. The program also allows for manual modifications, which were necessary in the emission lines. Our best guess of the true emission profiles are shown in Figures 1 and 2. In the spectrum of Q0107−025A, we did not attempt to fit between the peaks of the O VI $\lambda\lambda1031$, 1037 emission lines, but we excluded the region from 2020–2032 Å in constructing the line list.

We searched for significant lines in the normalized spectra using the interactive line-finding and fitting software of T. Aldcroft, which uses algorithms similar to the *HST* Quasar Absorption Line Key Project (cf. Schneider et al. 1993). The instrumental line spread function (LSF) was convolved with the data and error arrays to get the equivalent width W_i and corresponding uncertainty $\sigma(W)_i$ of an unresolved line at each pixel. The regions satisfying the criterion $W_i/\sigma(W)_i > 3.5$ were flagged as candidate lines. All the candidate absorption lines were then fitted in an interactive manner by single or, in the case of obvious blends, multiple Gaussians unconstrained in FWHM, equivalent width, and central wavelength. The signal-to-noise ratio defined according to the Key Project as (Schneider et al. 1993)

$$\text{SNR} = \frac{W}{\sigma(W)},$$

where W is the measured equivalent width and $\sigma(W)$ is the 1 σ uncertainty in the equivalent width was computed for each line and those absorption features with SNR ≥ 3.5 were included in the line lists for Q0107−025A and B given in Tables 3 and 4, respectively. These lists were useful in identifying the absorption lines in these spectra as well as the GHRS data. Below, we define subsamples of 3.5 σ and 5 σ Lyα absorption lines drawn from these line lists for use later in our likelihood analyses of the characteristic size of Lyα absorbers.

In a number of cases, the best fit to a line was a single Gaussian with an unphysically large FWHM. [Doppler widths determined by fitting Voigt profiles to Lyα lines in echelle spectra are typically less than $b = 60$ km s^{-1} (Hu et al. 1995).] Unless the line-finding software separated it into multiple components, a feature was counted as a single line in Tables 3 and 4, although in higher resolution data the feature would likely be resolved into narrower components. Only in those cases where the blended components were flagged by the line selection software did we attempt a multicomponent fit, and then only when the reduced χ^2 of the fit was smaller for the multicomponent fit than for a single Gaussian. There were also cases where the FWHM of

Number	λ_{obs} (Å)	σ_λ (Å)	W_{obs} (Å)	σ_W (Å)	SNR	FWHM	ID	z_{abs}	Remarks
1	1637.98	0.38	1.37	0.38	3.6	2.99	C II 1334	0.2274	
2	1671.76	0.15	0.98	0.15	6.5	1.96	Al II 1670	0.0006	
	1671.76	0.15	0.98	0.15	6.5	1.96	Lyγ	0.7190	
3	1683.81	0.10	1.22	0.14	8.6	1.87	Lyα	0.3851	
4	1688.70	0.14	0.65	0.12	5.4	1.50	Lyα	0.3891	
5	1697.16	0.25	0.53	0.13	3.9	2.04	Lyδ	0.7870	
6	1701.94	0.18	0.73	0.13	5.6	2.11	Lyα	0.4000	a
7	1722.10	0.19	0.86	0.16	5.4	2.24	Lyα	0.4166	b
8	1728.30	0.37	0.80	0.20	4.0	3.21	Lyα	0.4217	c
9	1738.77	0.08	0.94	0.10	9.6	1.70	Lyγ	0.7879	
	1738.77	0.08	0.94	0.10	9.6	1.70	Lyη	0.8773	
10	1747.08	0.16	0.32	0.09	3.7	1.30	Lyζ?	0.8771	
11	1760.58	0.18	0.47	0.10	4.6	1.71	Lyϵ	0.8773	
12	1763.94	0.10	0.87	0.11	8.0	1.66	Lyβ	0.7197	
13	1774.16	0.17	0.54	0.10	5.6	1.98	Lyβ	0.7297	
14	1782.75	0.09	0.58	0.08	7.6	1.43	Lyδ	0.8771	
15	1809.50	0.29	0.44	0.11	3.9	2.40	Lyα?	0.4885	
16	1825.62	0.05	1.84	0.09	21.1	2.41	Lyα	0.5017	
	1825.62	0.05	1.84	0.09	21.1	2.41	Lyγ	0.8772	
17	1833.36	0.15	0.54	0.09	6.1	1.93	Lyβ	0.7874	
18	1867.83	0.04	2.73	0.09	30.7	2.61	Lyα	0.5365	
19	1894.36	0.10	0.98	0.09	11.4	2.28	Lyα	0.5583	d
20	1900.66	0.11	0.51	0.07	7.3	1.42	C IV 1548	0.2277	e
21	1904.13	0.10	0.49	0.07	6.8	1.62	C IV 1550	0.2279	e,f
22	1912.11	0.20	0.30	0.07	4.2	1.71	Lyα?	0.5729	g
23	1921.88	0.16	0.45	0.10	4.8	1.78	Lyα	0.5809	
24	1925.53	0.05	0.74	0.06	11.9	1.40	Lyβ	0.8772	
25	1956.36	0.25	0.36	0.09	4.2	2.00	Lyα?	0.6093	h
26	1976.83	0.21	0.32	0.07	4.4	1.87	Lyα?	0.6261	h
27	1987.04	0.30	0.48	0.09	5.3	3.31	Lyα	0.6345	h
28	1995.02	0.09	0.54	0.07	8.1	1.55	C IV 1548	0.2886	i
29	1998.83	0.16	0.24	0.06	4.3	1.39	C IV 1550?	0.2889	i
30	2007.65	0.10	0.41	0.06	7.2	1.45	Lyα	0.6515	j
31	2016.22	0.07	0.65	0.07	9.9	3.30	Lyα	0.6585	k
32	2036.73	0.33	0.36	0.07	5.1	3.40	Lyα?	0.6754	l
33	2042.17	0.06	0.50	0.04	11.9	1.41	Lyα	0.6799	
34	2055.16	0.08	0.48	0.05	10.3	1.76	Lyα	0.6906	
35	2060.79	0.13	0.24	0.05	5.3	1.36	Lyα	0.6952	
36	2083.00	0.17	0.19	0.05	4.0	1.37	Lyα?	0.7135	l
37	2090.33	0.03	1.64	0.05	32.7	2.22	Lyα	0.7195	
38	2102.14	0.03	1.26	0.05	27.5	1.82	Lyα	0.7292	
39	2167.37	0.23	0.31	0.06	5.1	2.40	C IV 1548	0.3999	m
40	2172.52	0.04	1.24	0.05	26.2	1.95	Lyα	0.7871	
41	2188.78	0.23	0.40	0.09	4.5	2.40	Lyα	0.8005	
42	2197.92	0.26	0.31	0.06	5.0	2.69	Lyα?	0.8080	
43	2230.44	0.23	0.22	0.05	4.2	2.03	Lyα?	0.8347	
44	2241.55	0.13	0.32	0.05	6.8	1.76	Lyα	0.8439	
45	2247.07	0.06	0.48	0.04	12.3	1.42	Lyα	0.8484	
46	2252.61	0.09	0.29	0.04	7.4	1.34	Lyα	0.8530	
47	2263.13	0.51	0.50	0.13	3.9	5.09	Lyα?	0.8616	n
48	2272.73	0.07	0.39	0.04	9.6	1.47	Lyα	0.8695	
49	2282.03	0.02	1.22	0.04	33.2	1.68	Lyα	0.8772	
50	2298.01	0.05	0.39	0.03	11.6	1.30	Lyα	0.8903	

[a] System contains absorption from heavy elements.
[b] Possible blend with Lyβ of $z = 0.6799$ system.
[c] Feature was not found by Key Project software JASON.
[d] Possible blend with Lyβ of $z = 0.8484$ system.
[e] Corresponding Lyα line present in GHRS spectrum of Q0107−025A.
[f] Uncertain identification. Possibly Lyγ ($z = 0.9579$) with redshift ~ 200 km s^{-1} longward of the emission redshift of QSO.
[g] Uncertain identification. Possibly Lyγ ($z = 0.9661$) with redshift ~ 1500 km s^{-1} longward of the emission redshift of QSO.
[h] Possibly Lyβ.
[i] Probable C IV doublet. Corresponding Lyα would not lie in available FOS or GHRS spectrum of Q0107−025A.
[j] Uncertain identification. Possibly Lyβ ($z = 0.9573$) with redshift ~ 200 km s^{-1} longward of the emission redshift of QSO.
[k] Uncertain identification. Possibly Lyβ ($z = 0.9657$) with redshift ~ 1500 km s^{-1} longward of the emission redshift of QSO.
[l] Possibly spurious.
[m] Doublet component C IV 1550 would be blended with Lyα system at $z = 0.7871$.
[n] Probable blend since FWHM of line is 5.09 Å. No attempt at deblending was made since individual components are not obviously visible. Feature may disappear with slight change in the continuum.

TABLE 4

ABSORPTION LINES OF Q0107−025B IN FOS DATA

Number	λ_{obs} (Å)	σ_λ (Å)	W_{obs} (Å)	σ_W (Å)	SNR	FWHM	ID	z_{abs}	Remarks
1	1671.62	0.13	0.89	0.15	6.0	1.60	Al II 1670	0.0005	
	1671.62	0.13	0.89	0.15	6.0	1.60	Lyγ	0.7188	
2	1701.52	0.07	1.31	0.12	11.2	1.72	Lyα	0.3997	a,b
3	1718.05	0.33	1.05	0.20	5.2	3.13	Lyα	0.4133	
4	1738.53	0.18	0.50	0.11	4.4	1.64	Lyγ	0.7876	
	1738.53	0.18	0.50	0.11	4.4	1.64	Lyη	0.8770	
5	1747.00	0.11	0.63	0.10	6.2	1.42	Lyζ	0.8770	c
6	1760.37	0.14	0.52	0.12	4.5	1.39	Lyγ	0.8101	
7	1763.05	0.09	1.58	0.16	10.2	2.19	Lyβ	0.7188	c
8	1782.72	0.21	0.48	0.13	3.7	1.45	Lyδ	0.8771	
9	1785.07	0.43	0.78	0.21	3.7	3.38	Lyα	0.4684	
10	1824.19	0.09	1.72	0.11	15.7	2.97	Lyα	0.5006	d
	1824.19	0.09	1.72	0.11	15.7	2.97	Lyγ	0.8757	
11	1833.85	0.19	0.36	0.09	4.0	1.61	Lyβ	0.7879	
12	1845.16	0.07	0.78	0.08	10.3	1.41	Lyα	0.5178	e
13	1853.22	0.12	0.49	0.09	5.4	1.44	Lyα	0.5244	
14	1856.20	0.10	1.20	0.11	11.0	2.28	Lyβ	0.8097	
15	1867.30	0.10	1.05	0.11	10.0	2.00	Lyα	0.5360	f
16	1891.86	0.23	0.32	0.09	3.5	1.64	Lyα?	0.5562	g
17	1919.84	0.24	0.62	0.11	5.6	2.68	Lyα	0.5792	
18	1925.28	0.08	0.97	0.09	11.2	2.05	Lyβ	0.8770	
19	1950.91	0.19	0.29	0.08	3.8	1.46	Si IV 1393?	0.3997	b,h
20	1957.02	0.21	0.47	0.10	4.7	2.15	Lyα	0.6098	i
21	1972.63	0.15	0.37	0.07	5.0	1.57	Lyα	0.6227	i
22	1997.88	0.28	0.49	0.11	4.7	2.85	Lyα	0.6434	i
23	2002.71	0.28	0.30	0.08	3.7	2.15	Lyα?	0.6474	i,j
24	2006.52	0.31	0.33	0.10	3.5	2.33	Lyα?	0.6505	i,j
25	2019.15	0.16	0.33	0.06	5.5	1.80	Lyα	0.6609	
26	2049.44	0.32	0.25	0.07	3.5	2.30	Lyα?	0.6859	
27	2055.24	0.12	0.34	0.05	6.2	1.48	Lyα	0.6906	
28	2084.30	0.10	0.55	0.06	8.9	1.92	Lyα	0.7145	
29	2089.55	0.03	1.37	0.05	27.6	1.75	Lyα	0.7188	
30	2119.07	0.29	0.23	0.07	3.6	2.14	Lyα?	0.7431	i
31	2126.15	0.16	0.30	0.06	4.9	1.66	Lyα?	0.7490	
32	2166.97	0.12	0.45	0.06	7.4	1.90	C IV 1548	0.3997	b
33	2170.79	0.15	0.38	0.07	5.4	1.88	C IV 1550	0.3998	b
34	2173.57	0.06	0.78	0.07	10.9	1.72	Lyα	0.7880	
35	2186.21	0.16	0.53	0.07	7.8	2.52	Lyα	0.7984	
36	2200.36	0.03	1.61	0.05	31.2	2.00	Lyα	0.8100	
37	2211.41	0.11	0.30	0.05	6.1	1.34	Lyα	0.8191	
38	2216.38	0.49	0.40	0.10	4.3	4.35	Lyα?	0.8232	
39	2227.65	0.08	0.48	0.05	9.3	1.57	Lyα	0.8324	
40	2231.05	0.12	0.38	0.05	6.9	1.65	Lyα	0.8352	
41	2247.36	0.22	0.27	0.06	4.5	2.00	Lyα?	0.8487	
42	2281.61	0.03	1.10	0.04	25.2	1.70	Lyα	0.8768	
43	2298.26	0.09	0.27	0.04	6.6	1.32	Lyα	0.8905	

[a] System contains absorption from heavy elements.

[b] Member of Lyman limit system. Higher order Lyman series lines Lyβ through Lyε present in GHRS spectrum of Q0107−025B.

[c] Component is too strong with respect to other lines in this system and is almost certainly a blend.

[d] Associated Lyγ present in GHRS spectrum of Q0107−025B.

[e] Possible blend with Lyβ of $z = 0.7984$ system.

[f] Possible blend with C II 1334 of $z_{LLS} = 0.3997$ LLS system.

[g] Possible blend with Lyβ of $z = 0.8487$ system.

[h] Si IV λ 1402, the other member of the doublet, appears to be present at 2.7 σ confidence level.

[i] Possibly Lyβ.

[j] Possibly spurious.

a line was narrower than that of the instrumental line spread function (LSF). A histogram of FWHMs showed a smooth distribution with a peak between 1.4 and 1.8 Å and a sharp cutoff at 1.3 Å. We included all the lines with FWHM above this cutoff, with the assumption that those lines with widths between 1.3 and 1.4 Å are probably real, but their profiles are artificially narrow because they are contaminated by noise or because the continuum has been fit too low across them. This represents a departure from the approach taken by the Key Project, where, for narrow lines, the widths of the fitted Gaussians are kept fixed at the instrumental LSF. Because we selected lines according to the Key Project definition of SNR, their approach would have overestimated the significance of the narrow lines by underestimating the uncertainty in the fit.

In order to evaluate the completeness and reliability of the line lists, we performed several tests on the data. First, an independent check of the line lists was made using the software "JASON" developed for the *HST* Quasar Absorption Line Key Project (cf. Bahcall et al. 1996, and references therein). We are grateful to B. Jannuzi for providing us with the JASON line lists. The program is fully

automated and therefore offers a less subjective approach to line selection and fitting. The JASON line lists were derived using the normalized data used to generate Tables 3 and 4. Therefore, a comparison of the lines selected and measured by the two programs should be independent of the continuum fit.

The original analysis detected 93 lines among the two lines of sight. The Key Project software recovered 92 of those lines and found an additional 18 lines not listed in Tables 3 and 4. Of the extra 18 lines, 15 were fitted by JASON with the widths of the Gaussians profiles fixed at the instrumental LSF, which, as discussed above, tends to overestimate the SNRs of the lines. Since the line widths were always allowed to vary in our analysis, those lines would not be expected to be included in our line lists. With the exception of one line with $W_{obs} \simeq 0.25$ Å, all the lines had equivalent widths less than 0.20 Å. The remaining three lines selected only by the independent check were fitted as single, broad features with line widths greater than 5 Å. In our analysis, these features were modeled by two components whose SNR did not exceed the 3.5 σ confidence level. The equivalent widths of the components were less than 0.20 Å. The only line not found by JASON (see footnote in Table 3) is located in the noisy part of the spectrum of Q0107−025A, shortward of 1800 Å.

Among the lines found by both searches, the central wavelengths and equivalent widths of the lines agree within the uncertainties in all but four cases. The discrepancies can all be traced to differences in the treatment of broad or blended features. The JASON fits can sometimes become unrealistically broad, since the program systematically increases the region in which a feature is being fitted if another line is found nearby. Using our interactive approach, we are able to exercise greater control in fixing the size of the fitting window, albeit at the loss of objectivity. This was really only a problem in noisy parts of the spectra, but, in a few cases, it caused the equivalent widths measured by the Key Project software to be significantly higher than those determined by us.

In order to evaluate the effect of continuum placement on the line lists, we dropped the continuum everywhere by 3%, as a means of providing a reasonable lower bound to the true continuum level in each spectrum, and we repeated the search for significant features. A number of lines dropped out of the sample, giving an indication of the lines that are most secure and independent of the continuum fit. The lines not found in the new search have been flagged by question marks in Tables 3 and 4. Typically, their equivalent widths are less than 0.36 Å; the three above this equivalent width are broad features and could be artifacts of the continuum fit. Finally, we inverted the spectra and again search for significant "emission" features. We found only three, all with equivalent widths less than 0.28 Å.

Based on these tests, we estimate the reliability of the line lists (i.e., the probability that a line in our list is real) above a rest equivalent width of ∼0.24 Å to be at least 90%. Similarly, we estimate the completeness (i.e., the probability that a real line is in our list) above a rest equivalent width of ∼0.24 Å to also be at least 90%.

2.2. The GHRS Spectra

2.2.1. Observations

In order to extend the redshift coverage of the Lyα lines along the sight lines toward Q0107−025A,B down to red-

shifts near zero, we obtained spectra with the HST Goddard High Resolution Spectrograph (GHRS) using the G140L grating and the large science aperture (LSA). The usable spectral range is from about 1220–1495 Å. These two objects (especially Q0107−025A) are faint and near the limit of what can reasonably be observed with HST at these far UV wavelengths. Consequently, the SNR for Q0107−025A is quite poor. Nevertheless, some interesting features have been observed.

Q0107−025B was observed on 1994 September 22 UT and Q0107−025A was observed on 1994 November 15 UT. Quarter diode substepping was used with the FP-SPLIT option. A total integration time of 9792 s was obtained for each object. The mean background rate was approximately 0.03 counts s^{-1} diode^{-1} and the SNR ranged from ∼3 at 1220 Å to a peak of 7 at 1350 Å and 4 at 1480 Å for Q0107−025B with corresponding SNR levels of ∼3, 4, and 3 for Q0107−025A. One pixel is approximately 0.14 Å, and the line spread function has been approximated by a Gaussian with a FWHM of 10 pixels yielding a spectral resolution of 1.4 Å, or a velocity resolution of ∼300 km s^{-1} (Gilliland 1994, and 1995, private communication). The spectra were reduced at the Goddard Space Flight Center using the IDL software developed by the GHRS team (Blackwell et al. 1993).

2.2.2. Selection of Significant Absorption Lines

The GHRS spectra of Q0107−025A,B are shown in Figure 3. The spectra have been smoothed using a three-pixel running boxcar for the purpose of display only; the original data were used in the selection of significant lines. From this figure it is immediately obvious that there is a Lyman limit in Q0107−025B that is missing (or very much weaker) in Q0107−025A. We have generated line lists using exactly the same procedure described in § 2.1.2. However, because of the low SNR of these spectra we have been less conservative and listed all absorption features with formal significance greater than only 3 σ. Table 5 shows the resulting line list with the columns for each object being, respectively, the line number, wavelength, formal 1 σ uncertainty in the wavelength due to counting statistics, the observed equivalent width and associated uncertainty, the formal SNR of the line, the proposed identification, and the redshift. The limits on the equivalent widths of lines that are not seen along one line of sight when they are seen along the other line of sight are also 3 σ limits. Clearly, the reality of some of the lines near the low end of the significance threshold must be treated with some caution and should be verified by obtaining better data in the future.[10]

Relative wavelength shifts between the GHRS spectra of Q0107−025A and B are somewhat uncertain. The difference in the interstellar C II λ1334 velocities between Q0107−025A and B (119 km s^{-1}) deviates by about 3 σ from the formal expected uncertainty in the difference. (The Si II λ1260 line in Q0107−025A gives an even more discrepant result but the profile is complex and noisy). We have therefore shifted the Q0107−025A wavelength scale by 119 km s^{-1} to the red to force agreement with the Q0107−025B wavelength scale.

Inspection of Table 5 shows that many of the stronger lines in Q0107−025B are associated with the higher Lyman

---

[10] Further observations of Q0107−025A,B with the GHRS G140L have been obtained in Cycle 6 and should significantly improve the SNR of the present data.

TABLE 5

ABSORPTION LINES OF Q0107−025A,B IN GHRS DATA

A								B								A−B
Number	λ_{obs} (Å)	σ_λ (Å)	W_{obs} (Å)	σ_W (Å)	SNR	ID	z_{abs}	Number	λ_{obs} (Å)	σ_λ (Å)	W_{obs} (Å)	σ_W (Å)	SNR	ID	z_{abs}	Δv (km s^{-1})
			<0.74					1 ……	1234.27	0.16	0.62	0.16	3.8	Lyβ	0.2033	
1 ……	1259.80	0.10	0.82	0.15	5.3	Si II 1260	−0.0005	2 ……	1260.61	0.07	0.58	0.11	5.5	Si II 1260	0.0001	−193 ± 29
			<0.58					3 ……	1274.29	0.11	0.32	0.10	3.2	Lyα	0.0482	
2 ……	1311.37	0.16	0.46	0.14	3.2	Lyα	0.0787									
			<0.62					4 ……	1312.73	0.09	<0.38	0.08	4.2	Lyε[b]	0.3998	
			<0.65					5 ……	1329.35	0.06	0.32	0.07	6.2	Lyδ[b]	0.3997	
3 ……	1335.03	0.14	0.44	0.14	3.2	C II 1334	0.0004	6 ……	1335.03	0.12	0.46	0.11	6.8	C II 1334	0.0004	0 ± 41
4 ……	1357.05	0.07	0.68	0.12	5.5	Lyα	0.1163	7 ……	1356.70	0.07	0.72	0.08	6.9	Lyα	0.1160	77 ± 22
			<0.73					8 ……	1361.19	0.12	0.56	0.14	5.1	Lyγ[b]	0.3996	
			<0.65					9 ……	1362.88	0.13	0.70	0.13	3.7	Lyα	0.1211	
			<0.61					10 ……	1404.13	0.11	0.47	0.12	6.6	Lyα	0.1550	
			<0.77					11 ……	1435.72	0.09	0.77	0.11	5.0	Lyβ[b]	0.3997	
			<0.89					12 ……	1459.29	0.10	0.55	0.15	7.1	Lyγ[c]	0.5005	
			<0.92					13 ……	1462.50	0.08	1.03	0.14	8.3	Lyα	0.2030	
5 ……	1492.21	0.24	1.17	0.37	3.2	Lyα[a]	0.2275	14 ……	1491.90	0.14	1.18	0.15	3.4	Lyα	0.2272	62 ± 56

NOTES.—This table lists lines detected at or above 3 σ confidence level. The wavelengths have been shifted to the red by 75 km s^{-1} in order to register them with the FOS data. Upper equivalent width limits are 3 σ confidence level.

[a] Associated C IV doublet present in FOS spectrum of Q0107−025A.

[b] Member of Lyman limit system. Associated Lyα and C IV doublet present in FOS spectrum of Q0107−025B.

[c] Associated Lyα absorption line present in FOS spectrum of Q0107−025B.
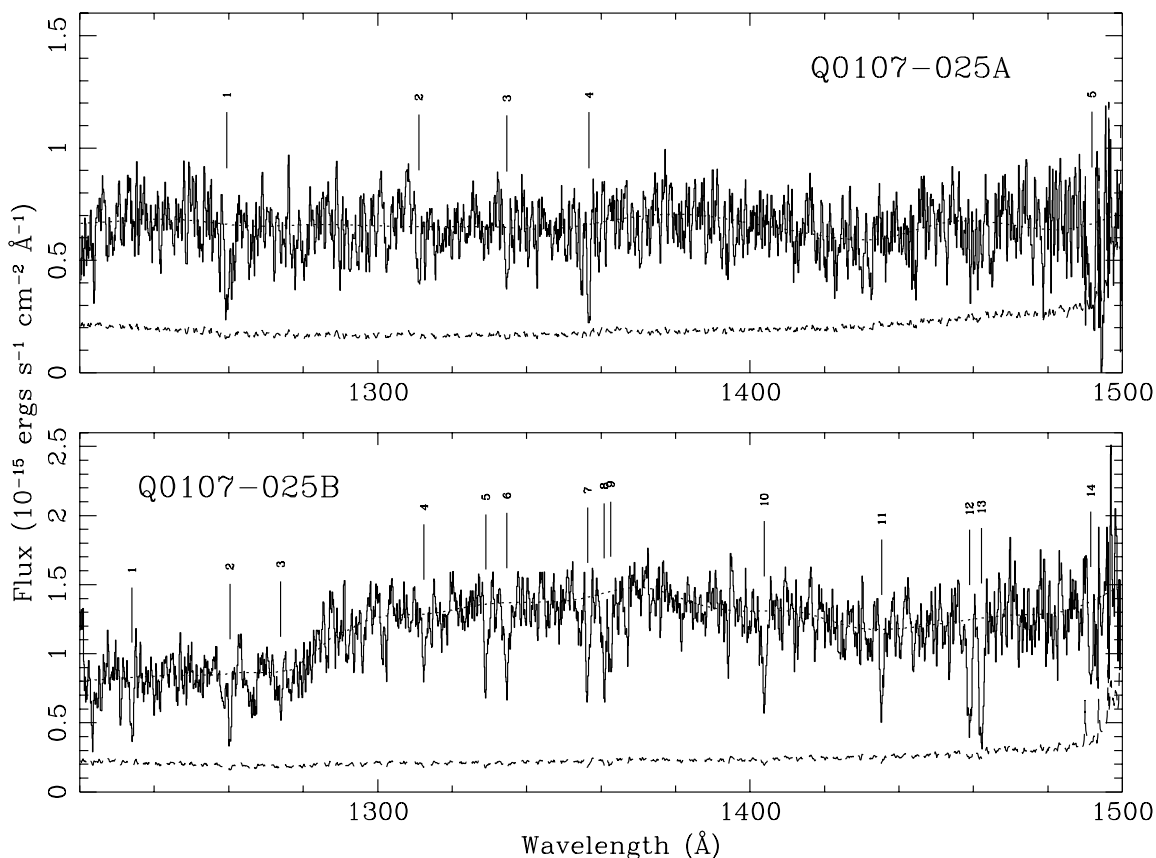
FIG. 3.—Spectra of Q0107−025A (*upper panel*) and B (*lower panel*) obtained with the *HST* GHRS as functions of vacuum wavelength. The dashed lines show the 1 σ errors in the fluxes, and the dotted lines represent the continuum fits. The spectra have been smoothed using a 3 pixel running boxcar.

series of the 1701.52 Å Lyα line in the FOS spectrum of Q0107−025B at a redshift of $z_{LLS} = 0.3997$. The measured redshifts of the Lyman series from β through ϵ were quite consistent among themselves, but they were shifted about 75 km s^{-1} to the blue relative to the wavelength scale for the FOS Q0107−025B observation. We therefore applied a shift of 75 km s^{-1} to the red to both the GHRS spectra (in addition to the 119 km s^{-1} shift to Q0107−025A noted above) to bring them into agreement with the FOS scale. *All these shifts have already been applied in Table 5.*

The optical depth of the Lyman limit in Q0107−025B was estimated by fitting the Q0107−025B continuum with a constant flux between 1300 and 1400 Å (corresponding to rest wavelengths in the Lyman limit system of 928 and 1000 Å), extrapolating it to shorter wavelengths, performing a similar fit between 1228 and 1270 Å (corresponding to rest wavelengths 877 to 907 Å) and measuring the ratio at rest 910 Å. We obtain an optical depth of 0.48 ± 0.06 corresponding to an H I column density of log $N(H\ \textsc{i})_B = 16.88 \pm 0.06$. The uncertainty is a rough estimate based upon slightly different fitting windows and fits made by three of us independently.

A similar fit to Q0107−025A gives a ratio of fluxes shortward and longward of the Lyman limit with an optical depth zero to within the errors. We estimate a conservative *upper* limit on the optical depth of the Lyman limit in Q0107−025A to be $\tau \simeq 0.1$, or log $N(H\ \textsc{i})_A \leq 16.20$. A simple naive *lower* limit on the column density toward Q0107−025A follows from assuming that the Lyα line in Q0107−025A is in reality a number of unsaturated components. This limit requires log $N(H\ \textsc{i})_A > 13.90$. Assuming

a single component with a Doppler parameter of 35 km s^{-1} would imply a value of log $N(H\ \textsc{i})_A = 14.52$. This would imply an equivalent width of the corresponding Lyβ line in Q0107−025A at 1435 Å of about 0.24 Å. There is no indication of a line at that wavelength; an unresolved line would have been only a 1.7 σ fluctuation.

We will adopt log $N(H\ \textsc{i})_A = 14.5$ as the approximate column density for the $z_{LLS} = 0.3997$ system toward Q0107−025A, bearing in mind the limits and corresponding large uncertainties just described.

2.3. *Ground-Based Spectra of Q0107−025A,B*

Optical spectra of the pair were obtained at the Multiple Mirror Telescope using the Blue Channel of the MMT Spectrograph equipped with a 3072×1024 optimized Loral CCD detector. Q0107−025A and B were observed for a total of 6600 and 4800 s, respectively, over the wavelength range 4150–5650 Å on 1994 September 29 and for 9600 and 5400 s in the range 3250–4250 Å on 1994 October 2. An 832 gpm grating was used in the second order on both nights along with a 1″ entrance slit; this combination gives a spectral resolution of 1 Å (FWHM). Data reduction followed standard procedures. Relative flux calibration was carried out using the spectrophotometric standard star Hiltner 600. Note that the standard was also observed through the narrow slit so that absolute fluxes derived from the spectroscopy will be unreliable. The resulting spectra are plotted in Figure 4.

The SNR of the ground-based spectrum is fairly low at the blue end of the spectrum (SNR $\simeq 3.5$ and 8 in Q0107−025A and B, respectively, at 3300 Å), but it reaches
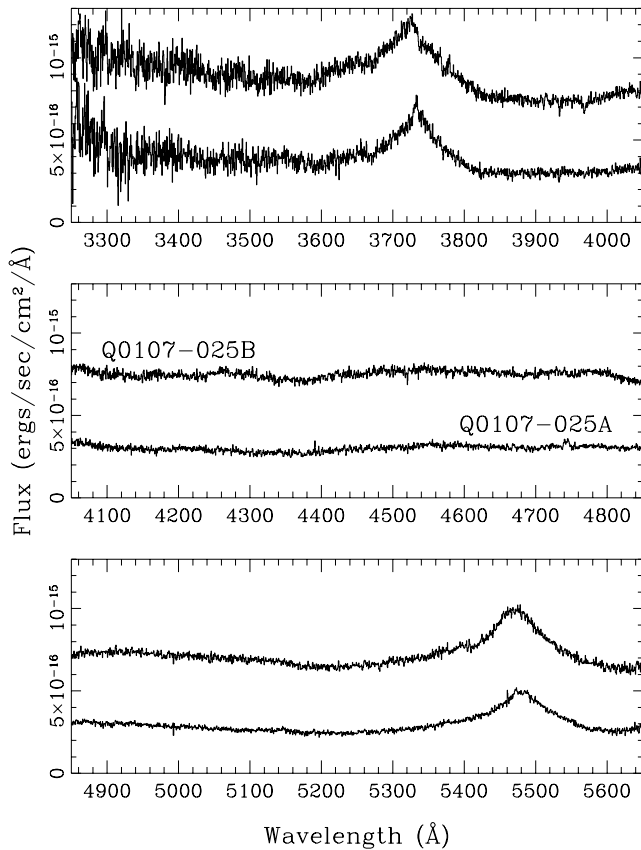
FIG. 4.—MMT spectra of Q0107−025A and B as functions of vacuum wavelength.

respectable values at wavelengths longward of about 3500 Å. The 5 σ observed equivalent width limit on a 2 Å wide line is about 0.6 and 0.33 Å at 3500 Å in Q0107−025A and B, respectively, 0.40 and 0.17 Å at 3750 Å, and less than 0.20 and 0.10 Å at all wavelengths longward of about 4000 Å.
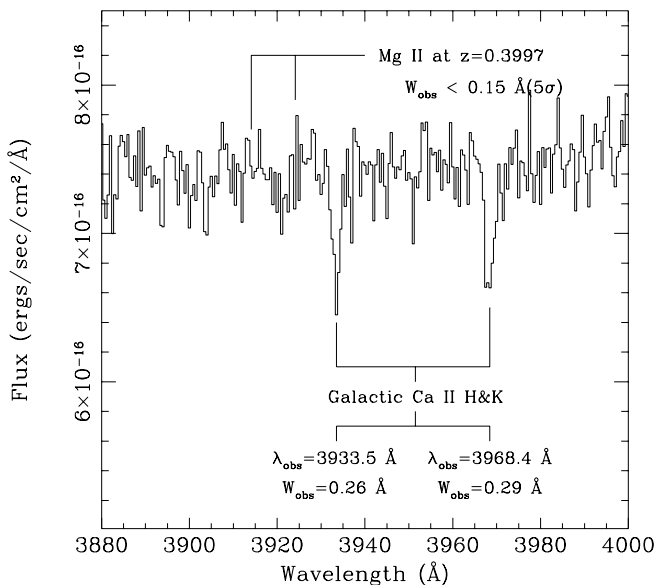

FIG. 5.—Expanded plot of the region of the spectrum of Q0107−025B, where Mg II absorption associated with the $z_{LLS} = 0.3997$ Lyman limit system would be expected to be seen. The 5 σ observed equivalent width limit in this region is about 0.15 Å, corresponding to a rest equivalent width limit of 0.11 Å. Note that this spectral region contains a saturated Ca II H and K doublet arising in the Galaxy.

The spectra were searched for significant lines that could correspond to Mg II $\lambda\lambda2796, 2802$ doublets from any of the systems identified from the *HST* data; none were found. A conservative statement is that no doublets could be identified at greater than the 5 σ confidence level with rest equivalent widths larger than 0.30 Å at redshifts larger than $z = 0.34$. Note that at the highest redshift corresponding to a common Lyα detection, $z = 0.877$, the 5 σ limits on the rest equivalent width of an individual line in a Mg II doublet are 0.08 and 0.05 Å for Q0107−025A and B.

An expanded plot of the region of the spectrum of Q0107−025B containing any Mg II absorption in the $z_{LLS} = 0.3997$ Lyman limit system is shown in Figure 5. The 5 σ observed equivalent width limit is about 0.15 Å, corresponding to a rest equivalent width limit of 0.11 Å. This spectral region in Q0107−025B contains a saturated Ca II H and K doublet arising in the Galaxy. However, the doublet is not seen in Q0107−025A. The galactic latitude of this sight line is $\sim 64°$, and if the clouds are at a distance of 300 pc, the linear separation of the sight lines is only 0.1 pc.

3. IDENTIFICATION OF ABSORPTION LINES

The line identifications posed a significant challenge given the limited spectral range and level of blending in the FOS data. We have followed closely the approach implemented in the Key Project program "*ZSEARCH*" for identifying the lines with the exception that our identifications were carried out manually. We used the set of UV absorption lines corresponding to the strongest transitions of the most abundant elements (Morton, York, & Jenkins 1988; Table 4). We first searched the spectra for Galactic interstellar lines. Then, starting from the red ends of the spectra, we searched for Lyα-Lyβ pairs with relative equivalent widths consistent with their known oscillator strengths. Since the spectra do not extend sufficiently redward to cover the Lyα emission lines of Q0107−025A and B, there are ambiguities in the identifications of the lines shortward of the Lyβ emission line; some of those lines could be Lyβ's for which corresponding Lyα's would not be observable. For this reason, searches for Lyβ-Lyγ pairs were also made. Finally, the spectra were scanned for doublets of C IV $\lambda\lambda1548, 1550$, Si IV $\lambda\lambda1393, 1402$, N V $\lambda\lambda1238, 1242$, and O VI $\lambda\lambda1031, 1037$. If any tentative metal features were identified, we searched for other plausible lines in the system.

In order for an identification to be accepted, we required that the discrepancy between the candidate and observed identifications had to be less than three times the estimated 1 σ uncertainty in the measured wavelength. In most cases, the agreement was considerably better. We also checked that the strengths of the absorption lines of the same ion identified within a given system were ordered according to the rules of atomic physics, taking into account uncertainties in the measured equivalent widths and well as possible blends. Therefore, if a candidate C IV doublet was identified, we checked that C IV $\lambda1548$ was stronger than C IV $\lambda1550$; and similarly for the doublets of Si IV, N V, and O VI; if candidate Lyman series lines were identified, we verified that their strengths decreased in the order: Lyα, Lyβ, Lyγ, Lyδ, etc.; and, finally, we checked that the strengths of candidate C II, N II, Si II, and Fe II lines were consistent with their known oscillator strengths.

Tables 3 and 4 list the parameters of the absorption lines detected in the FOS spectra of Q0107−025A and B, respec-

tively, including the central vacuum wavelengths and their 1 σ uncertainties, the equivalent widths and their 1 σ uncertainties, the SNRs and FWHMs, the proposed identifications, and finally the absorption redshifts. There are a number of cases in which a line was multiply identified. In these cases, both identifications have been listed in the tables. We found 50 absorption lines above the 3.5 σ equivalent width threshold in the FOS spectrum of Q0107−025A, 34 of which are Lyα absorption systems. In addition we identified three C IV doublet systems, one with associated Lyα absorption. In the other two cases, Lyα was not observable. In the FOS spectrum of Q0107−025B, a total of 43 absorption lines was detected and 31 Lyα absorption systems identified, one with associated metal lines.

The lack of spectral coverage out to the Lyα emission lines of the QSOs makes the identifications of some of the lines shortward of the Lyβ emission features uncertain. In particular, there are two possible Lyβ-Lyγ pairs in the spectrum of Q0107−025A with velocities of 200 and 1500 km s^{-1} longward of the emission redshift. (The alternate identifications are noted in Table 3.) Because a redshift with respect to the Lyα emission of 1500 km s^{-1} is larger than typically observed for Lyα systems and because the strengths of the lines belonging to the Lyβ-Lyγ pairs are inconsistent with their f-values, we chose to identify the lines as Lyα, with the exception of one line, which was identified as a member of a probable C IV system. Observations out to the Lyα emission lines are required to confirm these identifications. Further *HST* observations in the spectral range 2225–3275 Å, obtained in Cycle 5, should resolve these, and other, ambiguities.

Two lines, located at 1825 Å in the spectra of both Q0107−025A and B and identified as Lyγ at $z_{abs} = 0.8772$ (A) and $z_{abs} = 0.8757$ (B), have equivalent widths twice that expected from the strengths of the Lyα and Lyβ lines corresponding to the Lyγ absorption. The lines show definite asymmetries and are likely blends. For this reason, we have given the lines a second identification of Lyα at $z_{abs} = 0.5009$ in Q0107−025A and $z_{abs} = 0.5004$ in Q0107−025B. We comment on these systems in greater detail in § 4.3.

The tentative identifications of two C IV systems in Q0107−025A are worthy of comment. The $z_{abs} \simeq 0.228$ system was identified by a C IV λλ1548, 1550 doublet and C II λ 1334 line. Lyα also appears to be present in the GHRS data of both Q0107−025A and B at the 3.2 σ significance level. Despite the presence of C II λ1334, lines from other low ionization ions, e.g., Si II, Fe II, Al II, and Al III, are all absent. Similarly, the Si IV λλ1393, 1402 doublet is not observed. We searched for the Mg II doublet in our ground-based data, but did not find it to a limiting equivalent width (3 σ) of 0.4 Å. From apparent structure in the C IV doublet lines, this system may break up into several components, but higher SNR is required to confirm this. The velocity difference of the system, based on the Lyα lines, is 62 ± 56 km s^{-1}.

The system at $z_{abs} \simeq 0.289$ was identified solely by the presence of the C IV doublet. Based upon the fact that Lyα is not accessible by our data and the strengths of the component lines agree with their oscillator strengths within the uncertainties of their measured equivalent widths, this system would be accepted according to the rules adopted for the Key Project. Moreover, the probability of getting an agreement of $\delta z \leq 0.0003$ between two lines by random chance is $[2 \times 0.0003/0.5] \times N_l = 6\%$, where $N_l = 50$ is the number of lines in the spectrum of Q0107−025A. Taking into account the fact that the probability of line ratio being ordered correctly is 0.5, the *a posteriori* probability of getting a C IV doublet purely by chance is even smaller, ∼3%.

4. CHARACTERISTICS OF THE ABSORPTION SYSTEMS

In § 4.1, we define two complete samples of Lyα absorption lines that we use in the next section to set limits on the size of the Lyα absorbers. In § 4.2, we derive a working definition of systems we consider common and not in common to the spectra of both Q0107−025A and B, and briefly comment on the common systems in § 4.3. Finally, in § 4.4, we discuss the metal-line and Lyman limit systems found in the spectra and comment on the limits that can be placed on the physical extent of those systems.

4.1. *Samples of Lyman-α Absorption Systems*

In this section, we construct two subsamples of Lyα absorptions lines from Tables 3 and 4, each having a different rest equivalent width detection limit. If we define the characteristic radius of an absorber in terms of the impact parameter that gives rise to a line with equivalent width above a given detection limit, then the subsamples can be used to estimate the cloud radii corresponding to different column densities. We did not include in these samples the absorption lines detected in the GHRS spectra, since those data are less homogeneous, although we found one new Lyα system and a possible second metal-containing system in common to both spectra (Table 5).

First, we define a sample of strong lines that we call the "strong-line" sample. This conservative list was published in Paper I and is reproduced in Table 6, with slight differences. This list consists of a complete sample of 5 σ lines with rest equivalent widths greater than 0.32 Å in the wavelength region 1800–2300 Å. Figure 6a shows the observed 5 σ equivalent width thresholds for unresolved lines as functions of wavelength for Q0107−025A and B. Most of the differences between Table 6 and the table in Paper I appear in the measured equivalent widths of the lines and reflect changes in the continuum fits, particularly in the emission features. In addition, Table 6 includes two probable Lyα absorption systems, not listed in the table of Paper I. The secure and strong lines that make up this list are unlikely to arise by statistical fluctuations; moreover, this list is likely to be essentially complete.

Because of the small size of the "strong-line" sample, we also define a larger, but less secure, sample of 3.5 σ lines, which we present in Table 7. We required lines in this sample to have rest equivalent widths greater than 0.24 Å, also in the wavelength range from 1800–2300 Å. Figure 6b shows the observed 3.5 σ equivalent width thresholds for unresolved lines as functions of wavelength for Q0107−025A and B. This "weak-line" sample is more likely to contain lines that are not real and to omit real lines than the "strong-line" sample.

The results of our analysis hinge on whether the absorption features are correctly identified as Lyα lines. The number of Lyα absorption features is consistent with other estimates of the line density. The FOS data have comparable SNR to those of the *HST* Quasar Absorption Line Key Project. Using the results of Paper I of the Key Project (Bahcall et al. 1993), we expect to see about 9 ± 3 Lyα systems in each QSO spectrum in the range 1800 ≤

TABLE 6

"Strong-line" Sample of Coincident and Anticoincident Lyman-α Systems

| | A | | | | | | B | | | | | | A–B |
Number	λ (Å)	σ_λ (Å)	W_0 (Å)	σ_W (Å)	SNR	z_{abs}	Number	λ (Å)	σ_λ (Å)	W_0 (Å)	σ_W (Å)	SNR	z_{abs}	Δv (km s⁻¹)
16	1824.54	0.10	0.40	0.07	5.8	0.5009	10	1823.94	0.10	0.89	0.09	9.6	0.5004	99 ± 23
			<0.24				12	1845.16	0.07	0.51	0.05	10.3	0.5178	
18	1867.83	0.04	1.78	0.06	30.7	0.5365	15	1867.30	0.10	0.68	0.07	10.0	0.5360	85 ± 17
19	1894.36	0.10	0.63	0.06	11.4	0.5583				<0.25				
			<0.20				17	1919.84	0.24	0.39	0.07	5.6	0.5792	
31	2016.22	0.07	0.39	0.04	9.9	0.6585				<0.16				
37	2090.33	0.03	0.95	0.03	32.7	0.7195	29	2089.55	0.03	0.80	0.03	27.6	0.7188	112 ± 6
38	2102.14	0.03	0.73	0.03	27.5	0.7292				<0.15				
40	2172.52	0.04	0.69	0.03	26.2	0.7871	34	2173.57	0.06	0.44	0.04	10.9	0.7880	−145 ± 10
			<0.12				36	2200.36	0.03	0.89	0.03	31.2	0.8100	
49	2282.03	0.02	0.65	0.02	33.2	0.8772	42	2281.61	0.03	0.59	0.02	25.2	0.8768	53 ± 5

Notes.—This table lists 5 σ lines with $W_0 > 0.32$ Å. Upper equivalent width limits are 5 σ confidence level. Lines numbers are the same as those given in Tables 3 and 4. As noted in Tables 3 and 4 and the text, line 16 in A and line 10 in B are blends. The wavelengths and equivalent widths of those lines given in this table are our best estimates based on fitting two Gaussian profiles to each of the blended features.

$\lambda \le 2310$ Å and with $W_0 > 0.32$ Å (effectively the criteria for a line to be included in the strong-line sample). We count seven such systems (plus an additional probable system) toward both Q0107−025A and B, consistent with the Key Project results.

4.2. Definition of Coincident and Anticoincident Systems

The close proximity of Q0107−025A and B allows an estimate of the transverse dimensions of the Lyα absorbers, based on the number of Lyα lines observed to be in common and not in common to both spectra. A line is defined to belong to a common, or coincident, system when a corresponding line is present in the other line of sight within some predetermined velocity difference. Conversely, a line is defined to be *not* in common, or anticoincident, if there is no corresponding line in the other line of sight within the same velocity difference. In this section, we establish the optimal velocity window for delineating coincident and anticoincident systems.

Ideally, we should be guided by the expected velocity dispersions between physically associated absorbing clouds, but there is little theoretical information or empirical evidence bearing on this question at this redshift. On the one hand, in a study to determine the relationship between Lyα
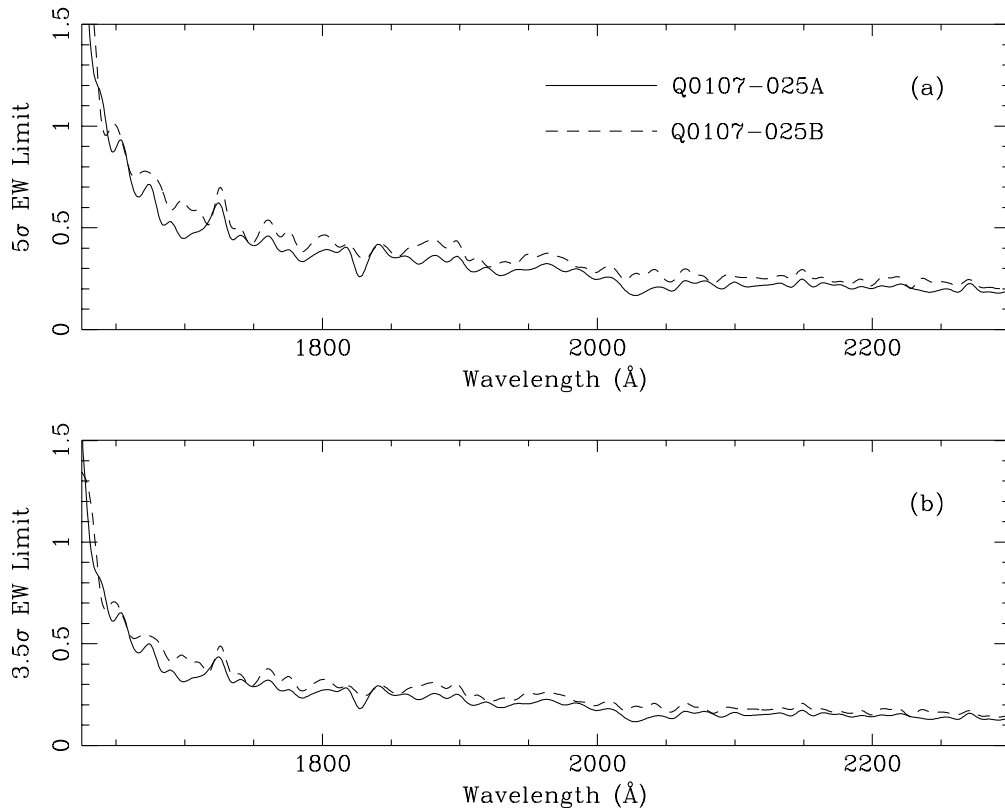

Fig. 6.—(a) Equivalent width thresholds (5 σ) for unresolved lines as functions of wavelength for the FOS spectra of Q0107−025A (*solid line*) and B (*dashed line*). (b) Same as (a), but here the equivalent width thresholds represent 3.5 σ confidence level.

TABLE 7

"Weak-line" Sample of Coincident and Anticoincident Lyman-α Systems

| | A | | | | | | | B | | | | | | A–B |
Number	λ (Å)	σ_λ (Å)	W_0 (Å)	σ_W (Å)	SNR	z_{abs}	Number	λ (Å)	σ_λ (Å)	W_0 (Å)	σ_W (Å)	SNR	z_{abs}	Δv (km s^{-1})
15	1809.50	0.29	0.30	0.07	3.9	0.4885				<0.17				
16	1824.54	0.10	0.40	0.07	5.8	0.5009	10	1823.94	0.10	0.89	0.09	9.6	0.5004	99 ± 23
			<0.16				12	1845.16	0.07	0.51	0.05	10.3	0.5178	
			<0.16				13	1853.22	0.12	0.32	0.06	5.4	0.5244	
18	1867.83	0.04	1.78	0.06	30.7	0.5365	15	1867.30	0.10	0.68	0.07	10.0	0.5360	85 ± 17
19	1894.36	0.10	0.63	0.06	11.4	0.5583				<0.17				
			<0.13				17	1919.84	0.24	0.39	0.07	5.6	0.5792	
23	1921.88	0.16	0.28	0.06	4.8	0.5809				<0.15				
			<0.13				20	1957.02	0.21	0.29	0.06	4.7	0.6098	
27	1987.04	0.30	0.29	0.06	5.3	0.6345				<0.13				
			<0.12				22	1997.88	0.28	0.30	0.07	4.7	0.6434	
30	2007.65	0.10	0.25	0.04	7.2	0.6515				<0.13				
31	2016.22	0.07	0.39	0.04	9.9	0.6585				<0.12				
33	2042.17	0.06	0.30	0.02	11.9	0.6799				<0.12				
34	2055.16	0.08	0.28	0.03	10.3	0.6906				<0.10				
			<0.09				28	2084.30	0.10	0.32	0.03	8.9	0.7145	
37	2090.33	0.03	0.95	0.03	32.7	0.7195	29	2089.55	0.03	0.80	0.03	27.6	0.7188	112 ± 6
38	2102.14	0.03	0.73	0.03	27.5	0.7292				<0.10				
40	2172.52	0.04	0.69	0.03	26.2	0.7871	34	2173.57	0.06	0.44	0.04	10.9	0.7880	−145 ± 10
			<0.08				35	2186.21	0.16	0.29	0.04	7.8	0.7984	
			<0.08				36	2200.36	0.03	0.89	0.03	31.2	0.8100	
			<0.08				39	2227.65	0.08	0.26	0.03	9.3	0.8324	
45	2247.07	0.06	0.26	0.02	12.3	0.8484				<0.09				
47	2263.13	0.51	0.27	0.07	3.9	0.8616				<0.08				
49	2282.03	0.02	0.65	0.02	33.2	0.8772	42	2281.61	0.03	0.59	0.02	25.2	0.8768	53 ± 5

Notes.—This table lists 3.5 σ lines with $W_0 > 0.24$ Å. Upper equivalent width limits are 3.5 σ confidence level. Lines numbers are the same as those given in Tables 3 and 4.

absorption and galaxies, Lanzetta et al. (1995) paired Lyα absorption lines with galaxies if their redshift agreements were better than 1000 km s^{-1}, though in practice, the velocity differences of most galaxy-absorption pairs were found to lie within 250 km s^{-1}; and Cristiani et al. (1995) have detected significant clustering of the high-redshift Lyα absorbers with N(H I) $\gtrsim 10^{14}$ cm^{-2} on scales out to 350 km s^{-1}. On the other hand, Dinshaw et al. (1994) found that a histogram of nearest-neighbor pairs of the lines in the QSO pair Q1343+2640A,B showed a peak within a velocity difference of 150 km s^{-1} and no additional pairs out to $|\Delta v| > 2000$ km s^{-1} (see also Fang et al. 1996). The smaller velocity window is also consistent with results of hydrodynamical simulations, which show the median velocity difference of common systems along adjacent lines of sight separated by several hundred kpc to be less than 100 km s^{-1} (Miralda-Escudé et al. 1996).

The velocity window we adopt must be a compromise between a velocity difference that is large enough to accept common systems that are physically related, but not so large that a significant number of coincidences arising by chance are included. We derived the optimal velocity difference for both the strong- and weak-line samples in the following manner: For each line in the spectrum of Q0107−025A, we calculated the velocity difference Δv between it and its nearest neighbor in the spectrum of Q0107−025B, requiring that each line belong to only one pair. We carried out the same analysis for 1000 samples of randomly placed absorption lines, distributed over the same range of wavelengths as the data samples. The simulated samples contained the same number of lines as the strong- and weak-line samples.

The velocity difference distributions of observed and expected "nearest-neighbor" pairs in bins of 50 km s^{-1} are shown in Figure 7 for the strong- and weak-line samples. The figure shows five pairs within a velocity difference of 150 km s^{-1}, including the probable common system at $z_{abs} \simeq 0.501$. The velocity separation of the probable system, $\Delta v = 99 \pm 23$ km s^{-1}, is uncertain because it was derived from blended lines (cf. § 4.3). In the strong-line sample, there are no additional pairs out to a velocity difference of ~4000 km s^{-1}. However, in the weak-line sample,
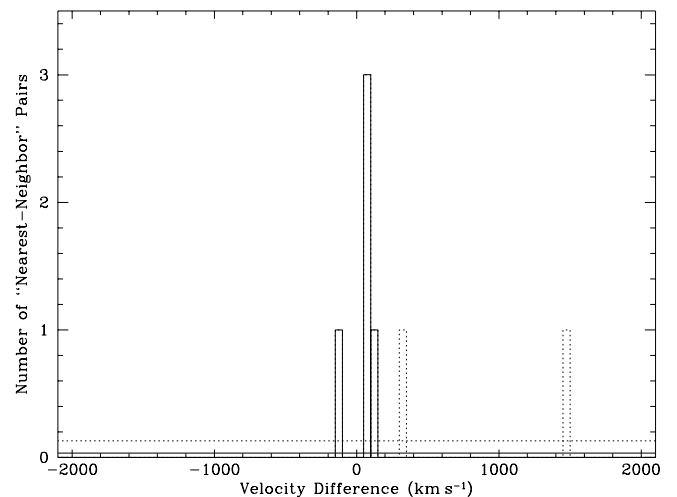

FIG. 7.—Distributions of "nearest-neighbor" pairs observed in Q0107−025A,B for the strong-line (solid histogram) and weak-line (solid and dotted histogram) samples. The expected numbers of pairs for the strong-line (solid line) and weak-line (dotted line) samples were estimated from 1000 samples of randomly placed absorbers.

Figure 7 shows a possible coincidence at a velocity difference of 320 km s^{-1}, and another at 1460 km s^{-1}. A velocity window of 1500 km s^{-1} is larger than that used in any other study and would include an unacceptable number of random coincidences. Within a velocity difference of 150 km s^{-1}, we expect 0.2 random coincidences in the strong-line sample, which contains eight lines per spectrum. This number grows to 0.8 for the weak-line sample, which contains approximately 16 lines per spectrum. For $|\Delta v| < 500$ km s^{-1}, the number of random pairs is 2.5, consistent with the possible sixth coincidence (with $\Delta v = 320$ km s^{-1}) in the weak-line sample arising randomly. As a practical matter, our experiments with different velocity windows always result in the five original pairs within a velocity difference of ± 150 km s^{-1}. Therefore, we adopt the criterion that lines corresponding to a coincidence must agree in velocity to within 150 km s^{-1}, consistent with similar studies of other QSO pairs (Dinshaw et al. 1994; Bechtold et al. 1994; Fang et al. 1996). Under this criterion, both samples have an identical number of coincidences; however, the number of anticoincidences is doubled between the strong- and weak-line samples.

The measured velocity differences among the coincidences range from -145 km s^{-1} to 112 km s^{-1} (Tables 6 and 7). The mean velocity difference is 26 km s^{-1}, smaller than the expected error due to mispointing of *HST*. The rms velocity difference about the mean is 104 km s^{-1}. (Including the one probable coincidence whose velocity difference is based on blended lines, the rms velocity difference is 97 km s^{-1}.) Assuming the uncertainties in the line fitting and wavelength calibration are random, the expected uncertainties in the radial velocity difference of a pair of lines is conservatively estimated to be ~ 17 km s^{-1}. We may therefore conclude that we are seeing statistically significant velocity differences over scales of several hundred kpc.

4.3. *Notes on Common Lyman-α Systems*

In this section, we comment on the common Lyα absorption systems found in the strong- and weak-line samples. We also include the one common (nonmetal-containing) system present in the GHRS spectra.

$z_{\rm abs} \simeq 0.116$. This common system is observed in the GHRS data. No lines associated with this system other than Lyα are detected. The velocity difference of the Lyα lines is 77 ± 22 km s^{-1}.

$z_{\rm abs} \simeq 0.501$. This is a probable common system, based solely on the presence of Lyα, which is severely blended with the Lyγ lines of the system at $z_{\rm abs} \simeq 0.877$ present in both spectra. We believe this is a common Lyα system because the strengths of the Lyγ lines are considerably stronger than the other lines identified with the $z_{\rm abs} \simeq 0.877$ systems, and the profiles show clear asymmetries. We have attempted to deblend the lines, although we did not list the deblended components in Tables 3 and 4, because the line selection software did not identify the components. Our best fits to the line profiles give Lyα components at 1824.54 ± 0.10 Å in Q0107$-$025A and 1823.94 ± 0.10 Å in Q0107$-$025B. Components at 1825.94 ± 0.05 Å and 1826.01 ± 0.20 Å correspond well to Lyγ lines belonging to the systems $z_{\rm abs} = 0.8772$ in Q0107$-$025A and $z_{\rm abs} = 0.8769$ in Q0107$-$025B, respectively. The velocity difference of the deblended Lyα components is 99 ± 23 km s^{-1}.

$z_{\rm abs} \simeq 0.536$.—This is a strong system for which only Lyα is observed. The higher order Lyman series lines would lie

shortward of the wavelength range covered by the FOS spectra, and none are seen in the GHRS data. The velocity difference is 85 ± 17 km s^{-1} for the system.

$z_{\rm abs} \simeq 0.719$.—This system contains Lyα, Lyβ, and Lyγ. The large equivalent width of Lyβ in the spectrum of Q0107$-$025B suggests that it is probably blended. The Lyγ's are both blended with Galactic Al II λ 1670 absorption. Given this blending, the system's velocity difference of 112 ± 6 km s^{-1} is based only on the Lyα lines.

$z_{\rm abs} \simeq 0.788$.—This system includes Lyα, Lyβ, and Lyγ. Lyδ is also seen in Q0107$-$025B but appears to blended with Lyη of the system at $z_{\rm abs} = 0.8772$. Si II λ 1193 and 1260 are possibly present in Q0107$-$025A, but such an identification is doubtful given the lack of Mg II absorption in the ground-based data. Neither Si II λ 1190 nor 1206 is observed, consistent with the oscillator strengths of Si II lines (Morton et al. 1988). The weighted average velocity difference of Lyα and Lyβ is -145 ± 10 km s^{-1}.

$z_{\rm abs} \simeq 0.877$.—In addition to Lyα, the higher Lyman series lines Lyβ through Lyθ are present in one or both QSOs. The equivalent widths of some of the lines are inconsistent with unblended Lyman series; Lyγ, Lyζ, and Lyη are certainly contaminated. The unblended lines give a weighted average velocity difference of 53 ± 5 km s^{-1}.

4.4. *Properties of the Metal-line and Lyman Limit Systems*

There are some additional features present in the FOS data that are of special interest in conjunction with the GHRS spectra. We observe a metal-containing system at $z_{\rm abs} \simeq 0.3997$ with a weak Lyman limit detected in Q0107$-$025B but not in A; in addition to the Lyα and the C IV doublet, we identified Si IV λ 1393 (Si IV λ 1402 appears to be present at the 2.7 σ significance level) along the sight line to Q0107$-$025B. C II λ 1334 is also possibly present in the spectrum of Q0107$-$025B but blended with Lyα at $z_{\rm abs} = 0.5360$. Lyα and C IV λ 1548 are seen in the spectrum of Q0107$-$025A but C IV λ1550 is blended with a Lyα at a different redshift. The system's velocity difference of 65 ± 25 km s^{-1} is based on the Lyα and C IV λ 1548 lines.

The fact that we see common Lyα (and possibly C IV) in the lines of sight to Q0107$-$025A and B, but the associated LLS is present only in Q0107$-$025B implies an upper limit on the diameter of the LLS of 250 h^{-1} kpc. We also have information about the relative transverse sizes of structures with very different column densities. From this system, it appears that the extent of the absorbing gas producing the Lyα and C IV systems is greater than that of the LLS, which is consistent with their relative cross sections derived from the statistics of the absorbers (cf. Steidel 1993). Since the LLSs are associated with higher column density material than the Lyα and C IV absorbers, this further implies that lower column density gas extends out to greater distances than higher column density gas. The equivalent widths of the Si IV and C II lines are too small to draw any conclusions on the linear extent of the absorbers producing them.

Using the prime focus spectrograph COSMIC on the Hale 5 m telescope and the multiobject spectrograph on the CFHT 3.6 m telescope, we have begun a survey of galaxies near the lines of sight to Q0107$-$025A and B in order to identify galaxies in the same volume of space as the Lyα absorbers seen in *HST* GHRS data. The objects have been selected using the galaxy classification software package FOCAS on an undispersed *V* image taken with the same spectrograph, and were chosen to be brighter than 21.5 *V*

magnitudes and to lie within a region of $8' \times 10'$ centered approximately on Q0107−025A,B. So far, we have obtained 31 redshifts. Although the redshift sample is still sparse, we observe several galaxies within $1\ h^{-1}$ Mpc of absorption systems in the GHRS data. We have so far failed to identify a galaxy that can plausibly be associated with the $z_{\rm LLS} = 0.3997$ Lyman limit system in Q0107−025B noted above. Either this galaxy is of rather low luminosity, or it is quite compact and nearly aligned with the QSO Q0107−025B and a more careful point spread function subtraction will be required for its detection. This work will be published in a forthcoming paper.

5. LIKELIHOOD ANALYSES

In this section, we use two maximum-likelihood techniques to estimate the characteristic size of the Lyα absorbers assuming a number of simple models. In § 5.1, we consider two geometries that are certainly too naive, but nevertheless are conceptually simple, namely, spherical absorbers and randomly inclined disks. We assume the absorbers are of uniform size and define the characteristic radius such that the nature of the column density distribution across the absorber is not important. In § 5.2, we present a new likelihood analysis that uses the information contained in the equivalent widths of the lines such that we can test the likelihood of three geometries: spherical clouds, with and without a range in size, randomly inclined disks and filaments. We assume the absorbers have power-law column density profiles.

5.1. *Simple Models*

As in Paper I, we assume the absorbers are coherent "clouds," since, with our current data set, we cannot really distinguish between coherent versus correlated structures. Aside from this basic assumption, the presence of common absorption systems in the lines of sight to Q0107−025A,B immediately implies a lower limit to the size of the Lyα absorbers, corresponding to the path length separation at the redshifts of the common systems. For the lowest redshift pair ($z = 0.536$), the lower limit on the *radius* of the absorbers corresponds to $140\ h^{-1}$ kpc and for the highest redshift pair ($z = 0.877$), it is $160\ h^{-1}$ kpc. The presence of a comparable number of features that are in common and not in common to both spectra suggests that we may be fortuitously sampling spatial scales that are of order of the characteristic size of the absorbers. We apply a maximum-likelihood analysis to the Lyα absorption line samples constructed in § 4.1 in order to determine the most probable radius of the Lyα forest absorbers assuming both spherical and disk geometries. For simplicity, we assume the absorbers are of uniform size, and we define the radius R of the absorbers to be the impact parameter that yields Lyα absorption above the detectability threshold of the sample being considered. The advantage of this approach is that we do not have to know or make any assumptions about the exact nature of the column density distribution across the absorbers.

The probability that a spherical cloud is intersected by both lines of sight, given that it is intersected by one line of sight is given by McGill (1990) as

$$\phi_s(X) = \frac{2}{\pi}\left\{\arccos\left[X(z)\right] - X(z)\sqrt{1 - X(z)^2}\right\}, \quad (1)$$

where $X(z) \equiv S(z)/2R$ and $S(z)$ is the line of sight separation at the redshift of the absorber. Note that equation (1) only holds for $0 \le X \le 1$ and is zero everywhere else. For disks, the probability is given by McGill (1990) as

$$\phi_d(X) = \int_{-\pi/2}^{\pi/2} \frac{\cos\theta}{\pi}$$
$$\times \left\{\arccos\left[\frac{X(z)}{\cos\theta}\right] - \frac{X(z)}{\cos\theta}\sqrt{1 - \frac{X(z)^2}{\cos^2\theta}}\right\}d\theta$$

(2)

for $X < \cos\theta$ and zero everywhere else.

At this point, we would like to correct an error made in Paper I, that was called to our attention by M. Fardal. In that paper, we used the probability ϕ_s to calculate the most probable radius. That probability addresses the question: "If a line appears in a *given* spectrum, what is the probability that a corresponding line appears in the other spectrum?" Therefore, only the anticoincidences from *one* line of sight should have been used, and *not* both lines of sight as was done in Paper I. Clearly, a disadvantage of using this probability is that it throws out valuable information. In order to incorporate all of the available information, we must define a probability that addresses the question: "If a line appears in *either* spectrum, what is the probability that a corresponding line appears in the other spectrum?" By simple geometrical arguments, this is easily shown to be

$$\psi_{s,d} = \frac{\phi_{s,d}}{2 - \phi_{s,d}}. \quad (3)$$

This error resulted in our estimating the radius of the clouds to be 40% smaller than if we had used the correct expression.[11]

The probability of getting the observed number of coincidences and anticoincidences is then given by the likelihood function (McGill 1990)

$$\mathscr{L}(R) = \prod_i \psi[X(z_i)] \prod_j \{1 - \psi[X(z_j)]\}, \quad (4)$$

where z_i is the redshift of the ith line "coincidence," and z_j is the redshift of the jth "anticoincidence."

The results of the likelihood analysis for both samples and geometries are summarized in Figures 8 and 9, and Table 8. In the strong-line sample, we count four coincidences and one probable coincidence. In addition, we observe three lines in each of Q0107−025A and B with no corresponding match. Figure 8 shows the likelihood distributions $\mathscr{L}(R)$ and their cumulative distributions for the strong-line sample assuming spherical absorbers and randomly inclined disks. From the peak of the likelihood distribution, the most probable radius for spherical absorbers is found to be $505\ h^{-1}$ kpc. From the cumulative distribution, we derive a median radius of $645\ h^{-1}$ kpc and 95% lower and upper confidence limits of $345 < R < 1520\ h^{-1}$ kpc. For randomly inclined disks, the cross section for both lines of sight intercepting a cloud is smaller than for spher-

---

[11] This led to a similar error in the Monte Carlo simulations performed in Dinshaw et al. (1994). There the cloud sizes were underestimated by 70%. The most probable radius for the Lyα absorbers in the lines of sight toward Q1343+2640A,B for the case of eight coincidences and four anticoincidences should be $125\ h^{-1}$ kpc with 95% confidence lower and upper bounds of $80 < R < 610\ h^{-1}$ kpc.
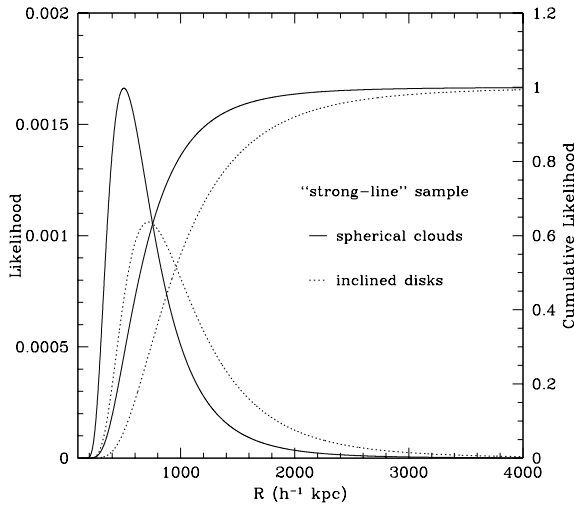
FIG. 8.—Likelihood distributions $\mathscr{L}(R)$ normalized by their integrated likelihoods for spherical absorbers (*sold curve*) and randomly inclined disks (*dotted curve*) as functions of cloud radius for the strong-line sample. The case shown is for five coincidences and six anticoincidences. The monotonically increasing curves represent the cumulative likelihoods from which the lower and upper bounds on the size of the Lyα absorbers have been derived. The cumulative likelihoods were obtained by integrating the likelihood distributions.
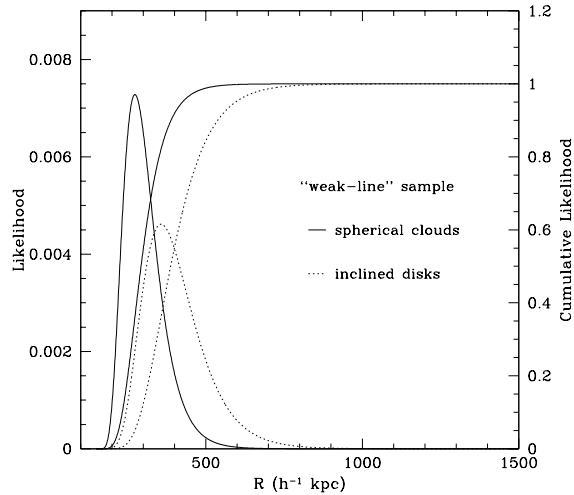
FIG. 9.—Same as Fig. 8, for the weak-line sample

ical absorbers, and the characteristic radius is correspondingly larger: $R = 715 \ h^{-1}$ kpc, with a median radius of 945 h^{-1} kpc and 95% confidence limits of $470 < R < 2310 \ h^{-1}$ kpc. Taking a conservative approach and not counting the one probable coincidence, we derive characteristic radii of 445 h^{-1} kpc, with 95% confidence limits of $310 < R < 1340$ h^{-1} kpc (spherical absorbers), and 625 h^{-1} kpc, with 95% confidence limits of $410 < R < 2025 \ h^{-1}$ kpc (disks).

Dropping the rest equivalent width threshold to 0.24 Å, we find no additional coincidences despite the fact that the number of lines detected in both lines of sight doubled. In total, we count five coincidences including the probable coincidence and 20 anticoincidences. The maximum-likelihood results for the weak-line sample are shown in Figure 9. For spherical absorbers, we derive a most probable radius of 275 h^{-1} kpc and a median radius of 295 h^{-1} kpc with 95% lower and upper bounds of $220 < R < 425$ h^{-1} kpc. For randomly inclined disks, the radius is found to be $R = 355 \ h^{-1}$ kpc with a median radius of 390 h^{-1} kpc and 95% confidence limits of $275 < R < 595 \ h^{-1}$ kpc. Excluding the one probable coincidence, the radii become 255 h^{-1} kpc with corresponding 95% confidence limits of $210 < R < 395 \ h^{-1}$ kpc (spherical absorbers), and 330 h^{-1} kpc with 95% confidence limits of $255 < R < 545 \ h^{-1}$ kpc (disks). We have assumed $q_0 = 0.5$; for $q_0 = 0$, the radii quoted are 20% larger (see Table 8).

The size estimates between the strong- and weak-line samples seem to suggest that the lower column density absorbers are *smaller* in extent than the high column density systems, contrary to what was found for the $z_{LLS} = 0.3997$ LLS (§ 4.4). Given that this result is not very significant and the fact that the weak-line sample likely contains lines that are not real (which would tend to bias the sample toward more anticoincidences), we hesitate to draw any conclusions at this time. Instead, we await further FOS observations of the pair in Cycle 5, which will raise the significance of many of the weaker lines and should help to resolve this issue.

5.2. Models with Power-Law Column Density Profiles

In this section, we present a new statistical technique, adapted from Maoz & Rix (1993), that utilizes the information in the equivalent widths of the lines in order to test the basic properties of the Lyα absorbers. This technique not

TABLE 8
RADIUS ESTIMATES OF THE LYMAN-α ABSORBERS

SAMPLE	N_{co}	N_{ac}	SPHERES R (h^{-1} kpc)	Median R (h^{-1} kpc)	95% Confidence Limits (h^{-1} kpc)	DISKS R (h^{-1} kpc)	Median R (h^{-1} kpc)	95% Confidence Limits (h^{-1} kpc)
"Strong-line" sample:								
$q_0 = 0.5$	4	6	445	575	310–1340	625	825	410–2025
	5	6	505	645	345–1520	715	945	470–2310
$q_0 = 0.0$	4	6	535	685	370–1605	745	985	495–2420
	5	6	600	770	410–1805	850	1120	560–2740
"Weak-line" sample:								
$q_0 = 0.5$	4	20	255	275	210–395	330	355	255–545
	5	20	275	295	220–425	355	390	275–595
$q_0 = 0.0$	4	20	310	330	255–475	395	430	305–655
	5	20	325	350	265–505	425	460	325–710

only provides an estimate of the radius of the absorbers, but allows us to test the relative likelihood of various geometric models. In this way, our method improves upon the diagnostic technique outlined by Charlton, Churchill, & Linder (1995) in that it provides a statistical basis for the tests. Much of the power of the technique comes from the fact that few observational points are required. However, there are limitations in both the data and the simple geometries considered, which we discuss below, that do not allow a definitive analysis at this time.

The degree of correlation between the rest equivalent widths of the common Lyα absorption lines toward Q0107−025A,B is shown in Figure 10. The first point to note about this figure is that the equivalent widths, W_A and W_B, exhibit significant deviations from unit slope ($W_A = W_B$), indicating a column density gradient within the absorbers on scales of several hundred kpc. As pointed out by Fang et al. (1996), there also appears to be a general trend toward larger equivalent width differences $|W_A − W_B|$ with max (W_A, W_B). Such a trend is consistent with coherent clouds having smooth column density distributions (Charlton et al. 1995), though the significance of this trend is not high given the small size of the sample. In contrast, no correlation between $|W_A − W_B|$ and max (W_A, W_B) is expected for clustered "cloudlets" since the column density is independent of radius (Charlton et al. 1995). Another feature of this plot worth pointing out is the lines detected in Q0107−025A appear to be stronger than those found in B. We do not yet understand the source of this, but we speculate it could be caused by uncertainties in the continuum placement, which would be exacerbated by the fact that the noise levels in Q0107−025A and B are not the same.

For simplicity and so that we can easily compare our results with those of Charlton et al. (1995), we assumed

absorber models with a power-law column density profile

$$N(r) = N_{\lim}\left(\frac{r}{R_0}\right)^{-\gamma}, \qquad (5)$$

where $N_{\lim}$ is the limiting column density of the sample being considered and R_0 is the radius of the absorber. We considered the cases $\gamma = 3, 4, 5, 6$, which correspond to column density distributions $f(N_{H I})dN_{H I} \propto N_{H I}^{-\beta} dN_{H I}$ with $\beta = 2, 1.67, 1.5, 1.33$, which bracket the power-law index of the observed column density distribution ($\beta = 1.7$; Rauch et al. 1993; Petitjean et al. 1995). We considered three geometries for the absorbers: spheres, randomly inclined disks, and pseudo-filamentary structures (approximated as disks with fixed inclination [cos $i = 0.2$]). Implicit in this definition is the fact that, for spherical clouds and filaments, the absorbers have constant radius, defined to be the impact parameter corresponding to $N_{\lim}$. For inclined disks, the column density increases across the absorber as sec θ (while the cross-sectional area of the absorber decreases as cos θ) and we must make the transformation $N_{\lim} \to N_{\lim}/\cos\theta$ in equation (5). Since the impact parameter at which $N_{\lim}$ is observed is greater depending on the inclination of the disk, the cross sections of the absorbers vary as the inclination. Obviously, for $r \to 0$, $N_{H I} \to \infty$; therefore a line of sight was never allowed to intersect the disk at an impact parameter smaller than that corresponding to a column density of $N_{H I} > 10^{20}$ cm^{-2}, which exceeds the largest observed column density.

For each model, we tested the set of parameters (e.g., R_0, γ) that predicts a particular distribution of pairs of column density or equivalent width along the two lines of sight. We then compared the observations with the simulated distribution to determine the best model or reject models. We evaluated the relative likelihood of these models using a likelihood function defined as

$$\mathscr{L} \equiv \sum_i \ln[p_i(W_1, W_2)] + \sum_j \ln[p_j(W_1, W_2 < W_{\lim})], \qquad (6)$$

where $p_i(W_1, W_2)$ is the probability that a particular model gives a coincidence with line equivalent widths W_1 and W_2, and similarly $p_j(W_1, W_2 < W_{\lim})$ is the probability that the model gives an anticoincidence with equivalent width W_1 in one line of sight and no detected line in the other, i.e., $W_2 < W_{\lim}$. Due to symmetries in the column density distributions, we arranged the observed and simulated equivalent widths such that $W_1 \equiv \max(W_A, W_B)$ and $W_2 \equiv \min(W_A, W_B)$. The most likely parameters for a given model were determined by maximizing the likelihood function, and their confidence intervals were derived from the relation $2(\mathscr{L}_{\max} − \mathscr{L})$, which is asymptotically distributed as a χ^2 distribution of n degrees of freedom, where n is the number of parameters considered simultaneously (Rix et al. 1996). The likelihood function in equation (6) provides insight into the relative likelihood of a model among those tested but does not provide a measure of the absolute likelihood of a given model.

5.2.1. The Column Density Distributions

The column density distribution along paired lines of sight for each of the geometric models considered was simulated by means of the Monte Carlo techniques outlined by Smette et al. (1992). For the spherical model, we randomly selected two points, r_A and r_B, separated by $S(z)$ corresponding to the separation between the lines of sight at redshift z,

FIG. 10.—Correlation between the rest equivalent widths, W_A and W_B, of the common lines in Q0107−025A and B, respectively. The dotted error bars represent the probable coincidence at $z_{abs} \simeq 0.501$. The equivalent widths associated with this coincidence are uncertain because they were measured using multicomponent fits to the lines. The dashed line has unit slope.

on a circular disk of radius $R_0 + S(z)$, where R_0 is the radius of the absorber. When either r_A or r_B happened to lie within the radius R_0 (such that a coincidence or anticoincidence was always obtained), the column densities at r_A and r_B were determined from equation (5). The simulations for randomly inclined disks and filaments were similarly carried out, but this time the geometry was that of ellipses on the sky with semimajor and minor axes of $R_0 + S(z)$ and $R_0/\cos \theta + S(z)$, respectively. For simplicity, we fixed the line-of-sight separation of the QSOs to be $S(z = 0.7) \simeq 300 \ h^{-1}$ kpc, despite the fact that our observations cover the redshift range $0.48 < z < 0.89$.

Figure 11 shows the loci of the column densities along the two lines of sight on plots of $\log N_A$ versus $\log N_B$ for spherical (*top panels*), pseudo-filamentary (*middle panels*), and disklike (*bottom panels*) absorbers. The dashed lines corresponds to the rest equivalent width threshold of the strong-line sample. The points lying above and to the right of the dashed lines represent coincidences, and those falling below the horizontal dashed line and to the left of the vertical dashed line represent anticoincidences. Points in the

unpopulated square box near the origin are disallowed by the condition that the column density along at least one line of sight be above N_{lim}. To illustrate the effect of varying R_0 and γ, the distributions have been derived for $R_0 = 300$, 1200, and 3000 h^{-1} kpc corresponding to 1, 4, and 10 times the line-of-sight separation of the QSO pair, and power-law indices of $\gamma = 4$ and 5. Immediately, we can see striking differences between panels.

The first point to note about Figure 11 is the presence of sharp boundaries delineating regions of significant and zero probability for both spherical and filamentary absorbers. This is in contrast to randomly inclined disks, which produce less well-defined boundaries because the column density across the disk and the effective radius of the disk depend on the inclination. Also apparent in Figure 11 is the fact that models involving spherical clouds with radii comparable to the line-of-sight separation cannot produce coincidences at large column densities, whereas anticoincidences at large column densities cannot arise in large spherical absorbers. Unlike the spherical absorber model, the region of nonzero probability density is spread over a larger area
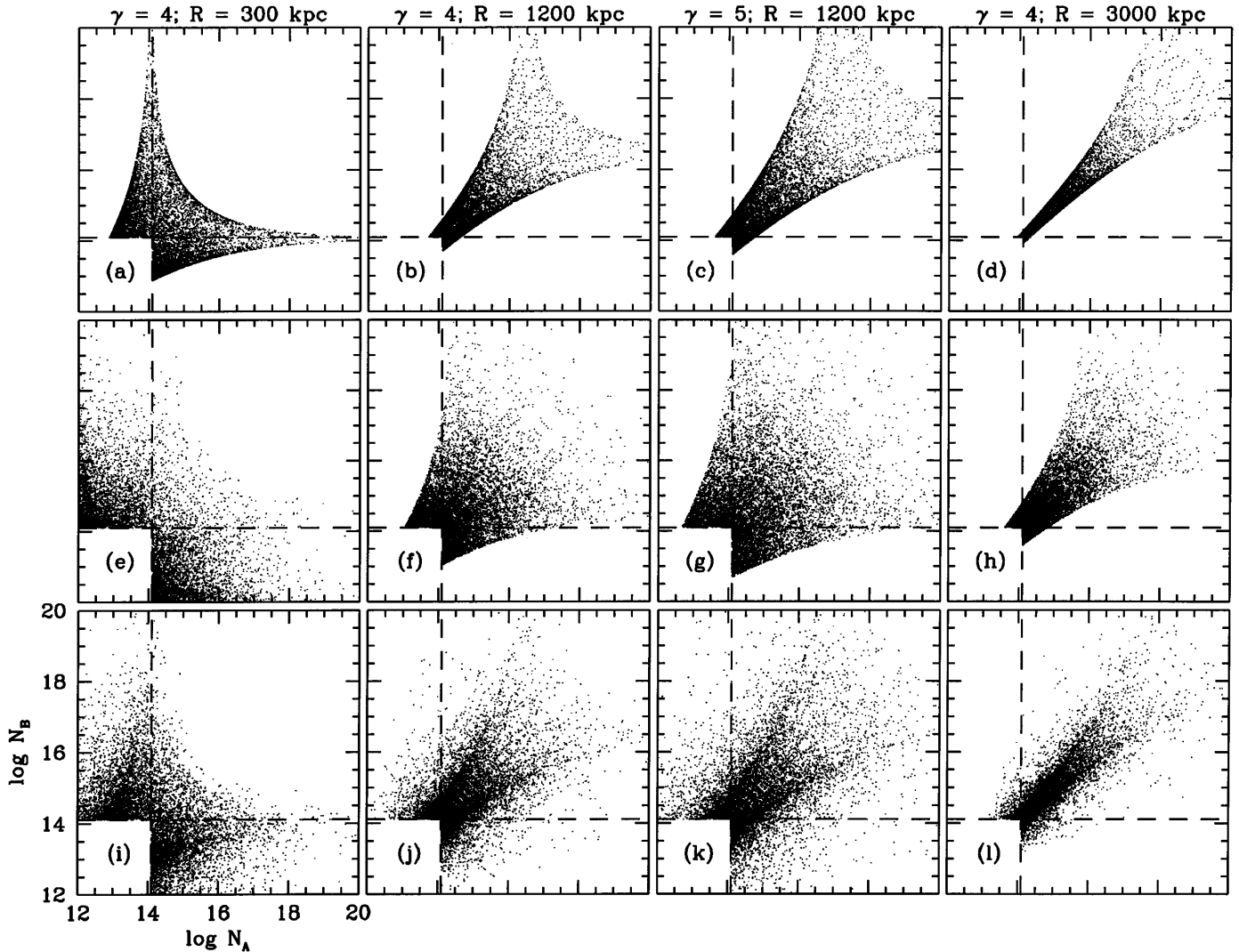

FIG. 11.—Column density distributions for spherical halo model (*top row of panels*), filamentary structures (*middle row of panels*), and randomly inclined disks (*bottom row of panels*). The dashed lines represent the column density threshold ($N_{\text{lim}} = 1.26 \times 10^{14}$ cm^{-2} for $b = 35$ km s^{-1}) for the strong-line sample. The points lying above and to the right of the dashed lines represent coincidences, and those falling below the horizontal dashed line and to the left of the vertical dashed line are anticoincidences. Points in the unpopulated square box near the origin are disallowed by the condition that the column density along at least one line of sight be above N_{lim}.

for a given radius for the filament and disk geometries. This is because inclined disks have larger column densities for given impact parameters and steeper N_{HI} profiles than face-on disks, such that a given line-of-sight separation samples a larger range of column densities. Therefore, it is possible to obtain *both* coincidences and anticoincidences at large column densities for absorbers with either a filament or disk geometry.

There are two features of the column density distributions that are independent of the geometry of the absorbers: (1) for radii progressively larger than the line-of-sight separation, the column densities become more highly correlated; and (2) for progressively larger γ (i.e., steeper drops in column density across the absorber), the cross section for detecting high column density systems increases, producing a greater spread in the probability density because a larger range of column densities is sampled.

5.2.2. Likelihood Limits

In order to compare the simulated distributions with the observations, we have plotted in Figure 12 the equivalent width distributions for spherical (*top panels*), pseudo-filamentary (*middle panels*), and disklike (*bottom panels*) absorbers. Superimposed on the simulated distributions are the equivalent widths of the observed coincidences and anti-coincidences for the strong-line sample. When the distribution of column densities is converted to the observable distribution in equivalent widths, the appearance of the diagrams changes quite dramatically and qualitatively new features appear arising from radiative transfer effects. In particular, the vertical ridges at $W_1 \simeq 1$ are caused by the transition from the flat part of the curve of growth (COG) to the square root part. In order to adequately populate regions of low probability that tended to occur at high column densities, the first impact parameter r_A was selected randomly from an exponential distribution [$r_A = \exp(x)$, where x was a random number between -10 and 0] and the points in the distribution weighted by r_A^2 to account for the nonuniform selection. We checked that this was correct by making sure we could recover the column density distribution with the value of β appropriate for the power-law exponent used. Because of this weighting, the regions of
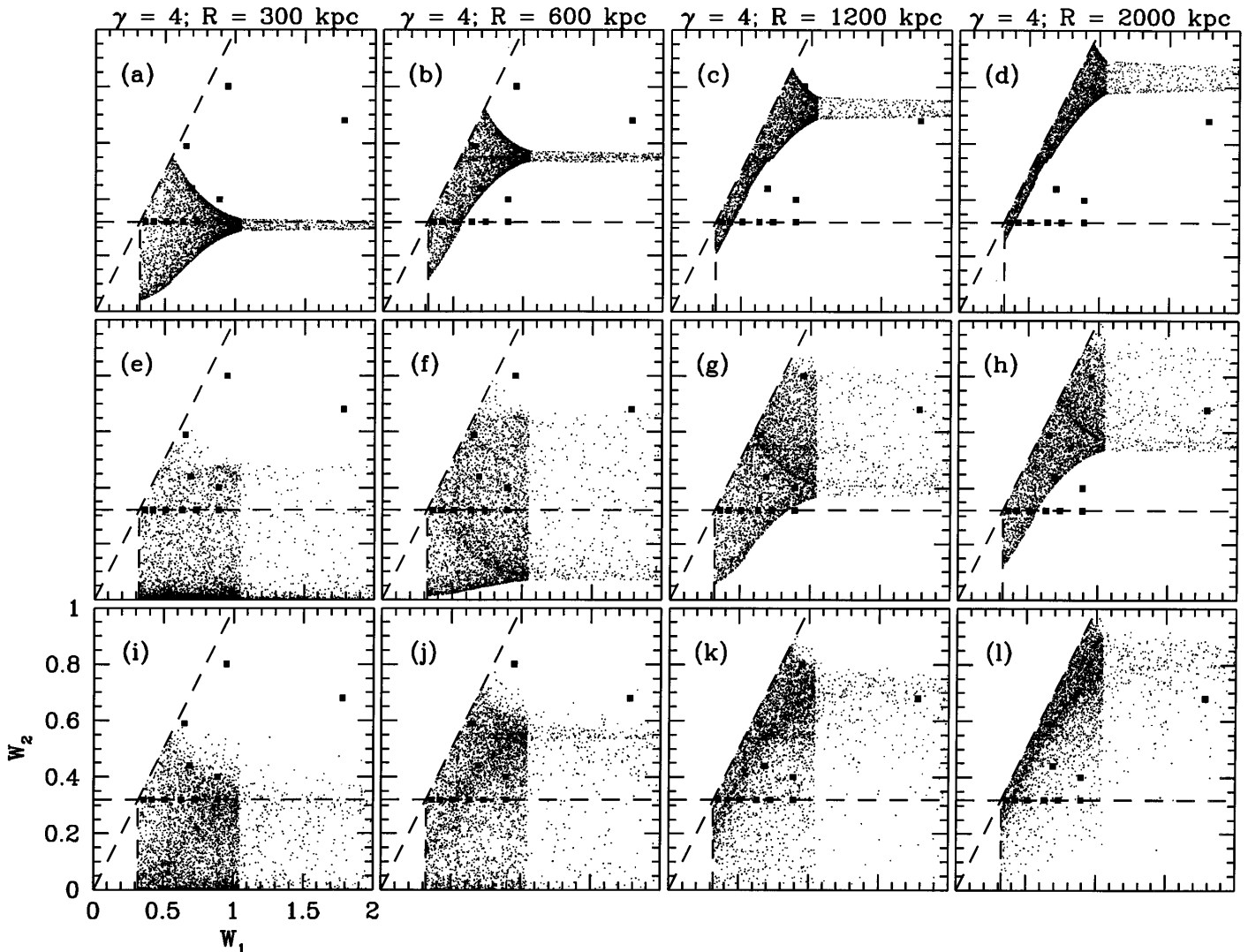

FIG. 12.—Equivalent width distributions for spherical halo model (*top row of panels*), filamentary structures (*middle row of panels*), and randomly inclined disks (*bottom row of panels*). The observed and simulated equivalent widths are arranged such that $W_1 \equiv \max (W_A, W_B)$ and $W_2 \equiv \min (W_A, W_B)$. The horizontal dashed lines represent the rest equivalent width threshold ($W_0 > 0.32$ Å) of the strong-line sample. The points lying above the dashed lines represent coincidences, and those falling below the horizontal dashed line are anticoincidences. Superimposed on the simulated distributions and indicated by the solid squares are the equivalent widths of the observed coincidences and anticoincidences for the strong-line sample.

nonzero probability in Figure 12 do not represent the true probability density.

The present data were obtained at a spectral resolution that does not allow a detailed COG analysis. Instead, we used an approximation having an accuracy of better than 10% to evaluate the COG in the range of optical depths from $0.1 \le \tau \le 40$ (Chernomodik & Ozernoy 1993):

$$W = \frac{\sqrt{2}b\lambda}{c}\left[\ln\left(1 + \frac{\pi}{2}\tau^2\right)\right]^{1/2}, \qquad (7)$$

where λ is the wavelength of the line, c is the speed of light, $\tau = 1.497 \times 10^{-2}\lambda fN/b$ is the optical depth, and $f = 0.416$ is the oscillator strength for the Lyα transition. The approximation provides a smooth transition between the linear and flat parts of the COG. For $\tau > 40$, we used the usual equations given in Spitzer (1978) to calculate equivalent widths. For simplicity, we also assume a single Doppler width of $b = 35$ km s^{-1}, which corresponds to the average b-value derived from several high-resolution studies of the Lyα forest at high redshift (Carswell et al. 1991; Rauch et al. 1993; Hu et al. 1995). For $b = 35$ km s^{-1}, the rest equivalent width limits of the strong- and weak-line samples correspond to $N_{\rm lim} = 1.26 \times 10^{14}$ cm^{-2} and 0.66×10^{14} cm^{-2}, respectively.

Figures 12a–12d show the equivalent width distributions for progressively larger spherical absorbers. The figure shows that *spherical absorbers with uniform radius provide a poor representation of the observed equivalent width distribution*. In particular, spherical clouds with radii less than $\sim 1000~h^{-1}$ kpc cannot reproduce the large equivalent width coincidences because the cross sections for producing the high equivalent width systems are smaller than the line-of-sight separation of Q0107$-$025A,B. Conversely, spherical absorbers with radii greater than $\sim 450~h^{-1}$ kpc cannot account for the large equivalent width anticoincidences. Charlton et al. (1995) have similarly ruled out spherical clouds as a possible model for the Lyα absorbers from observations of the $z \simeq 2$ QSO pair Q1343$+$2640A,B.

The equivalent width distributions for pseudo-filamentary absorbers and randomly inclined disks are shown in Figures 12e–12h and 12i–12l, respectively. For both models, there is a single radius for which all the observed coincidences and anticoincidences fall onto the region of nonzero probability. We evaluated the model that best represents the observations from the likelihood function in equation (6), where the probabilities were calculated using equivalent width distributions similar to those shown in Figure 12. The probability for each coincidence $p_i(W_1, W_2)$ was determined by counting the number of points in a square region containing that coincidence. A square was 0.08 Å on a side, corresponding to the typical uncertainty in the observed equivalent widths. The probability for each anticoincidence $p_j(W_1, W_2 < W_{\rm lim})$ was obtained by counting the number of points in a 0.8 Å wide vertical swath containing that anticoincidence. Each point was weighted according to r_A^2, as described above, and the probabilities were normalized by the sum of all the weights. We found that highly inclined disks (whose major axes can get very large) sometimes gave very large weights that dominated the sum, and produced statistically meaningless fluctuations in the probabilities even for very large numbers of realizations. To alleviate this problem, we restricted the inclinations of the disks to lie in the range $0.1 < \cos i < 1$.

The likelihood functions for filaments and disks are shown as functions of R in Figures 13 and 14, respectively, for exponents $\gamma = 3, 4, 5$, and 6. Large jumps or drops in the likelihood function occur when an observed coincidence or anticoincidence falls into or out of the region of nonzero probability density (regions outside those populated by points were assigned a probability of 10^{-12} in order to avoid the problem of equation (6) becoming indeterminate). The most probable values of γ and R were determined by maximizing the likelihood function $\mathscr{L}$. From Figures 13 and 14, $\gamma = 6$ corresponding to the steepest $N_{\rm H\,I}$ profile best reproduces the observed equivalent width distribution for both the filament and disk models. The most probable radii for the two absorber geometries were determined by fitting a parabola to the $(4~\sigma)$ peaks of the likelihood functions corresponding to $\gamma = 6$. For both the strong- and weak-line samples, the characteristic radius for the pseudo-filamentary geometry is 1150 h^{-1} kpc along the major axis, corresponding to 230 h^{-1} kpc along the minor axis. The 95% confidence lower and upper bounds on the major axis are $850 < R < 1465~h^{-1}$ kpc; the bounds on the minor axis scale by a factor of $\frac{1}{5}$. For the disk model, the most probable radius determined for the strong-line sample is 915 h^{-1} kpc with 95% confidence lower and upper bounds of $560 < R < 1270~h^{-1}$ kpc. The most probable radius for the weak-line sample is 1025 h^{-1} kpc with 95% confidence limits of $690 < R < 1360~h^{-1}$ kpc. From this likelihood analysis, we find that filaments and randomly inclined disks
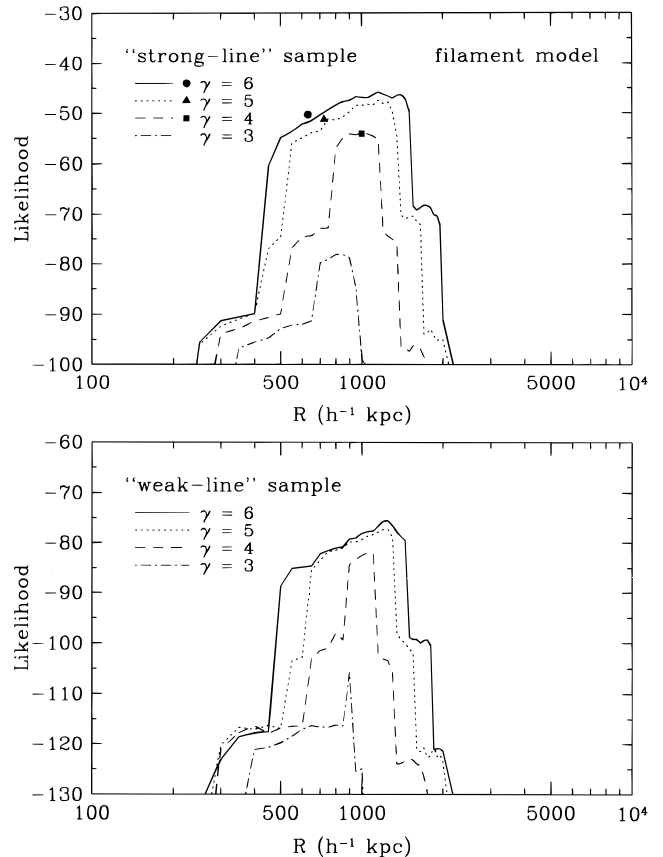

FIG. 13.—Likelihood functions for pseudo-filamentary absorbers with power-law column density profiles $N(r) \propto r^{-\gamma}$ for $\gamma = 3, 4, 5, 6$. Superimposed on the plots in the upper panel and indicated by points are the maximum-likelihood estimates for spherical absorbers with a power-law distribution of radii with index $\alpha = 3$ for three values of γ.
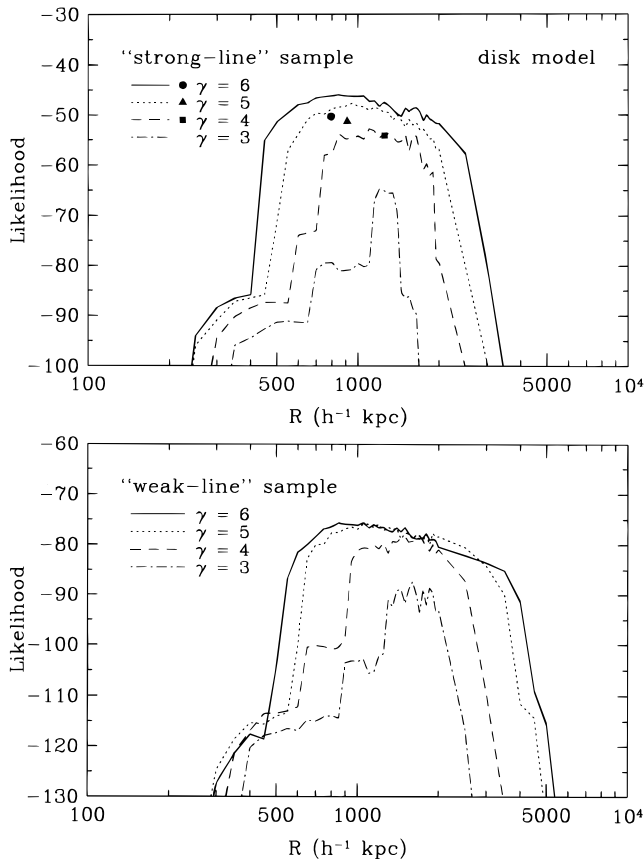
FIG. 14.—Same as Fig. 13, for randomly inclined disks

match the data comparably well, with disks only slightly favored over filamentary absorbers.

Finally, we tested whether spherical clouds with a range of sizes are consistent with the observations. We randomly selected radii according to two distributions: (1) exponential, and (2) power law with indices $\alpha = -4, -3, \ldots, 5, 6$. Spherical absorbers with an exponential size distribution gave a poor representation of the observations. For the power-law distribution, the likelihood as a function of α is a parabola with the peak likelihood at $\alpha = 3$. In Figures 13 and 14, we have superimposed on the likelihood functions for pseudo-filaments and randomly inclined disks the maximum-likelihood estimates for power law index $\alpha = 3$ only and for three values of γ. Although a model involving spherical absorbers with a range of sizes provides a reasonable representation of the observed equivalent width distribution, filamentary and disklike absorbers are favored over spherical clouds with a distribution of sizes at the 3 σ confidence level.

The most important result of this analysis is that the model that reproduces the observed equivalent width distribution best corresponds to the least restrictive geometry considered, i.e., randomly inclined disks. The implication of this result is that the Lyα absorbers are diverse structures. Randomly inclined disks give a range of cross sections and projected sizes depending on their inclination that eliminate the sharp edges and forbidden regions produced by spherical structures and filaments of a single size. This is consistent with the picture of Lyα absorbers derived from recent hydrodynamical simulations, where Lyα absorption is produced in the extended halos of galaxies and some arise in

the filaments and sheets between galaxies (Cen et al. 1994; Hernquist et al. 1996; Miralda-Escudé et al. 1996).

Although we have chosen in this paper to model the Lyα absorbers with power-law column density profiles, the likelihood technique presented here can easily be expanded to test other models, such as exponential disks with central column densities selected according to the observed column density distribution. Future analysis should also account for the error associated with the observed equivalent widths by convolving the probabilities, $p_i(W_1, W_2)$ and $p_j(W_1, W_2 < W_{\lim})$, with a distribution of errors in measured equivalent widths. This likelihood technique can also be expanded to include the information contained in the velocity differences of the common systems in order to diagnose the kinematics of the absorbers.

6. SUMMARY AND DISCUSSION

We have obtained *HST* observations with the FOS and GHRS of the QSO pair Q0107−025A,B in an attempt to measure the transverse size of the Lyα absorbers. In addition, ground-based observations have been obtained from 3200 Å to the Mg II emission redshifts of the QSOs in order to look for possible metal lines associated with the Lyα lines. From the presence of common absorption in the FOS spectra, we obtained lower limits on the radius of the clouds of 140–160 h^{-1} kpc. The presence of anticoincident systems allowed a measure of the characteristic size of the Lyα absorbers. We defined two samples of Lyα absorption lines, and estimated the most probable radius of the absorbers for both samples assuming two simple geometries. Defining a coincidence to be the case where Lyα absorption appears in both spectra within a velocity difference of 150 km s^{-1}, we counted five coincidences (including a probable coincidence) and six anticoincidences in the sample of strong lines with rest equivalent widths $W_0 > 0.32$ Å. Using a simple maximum-likelihood analysis, we obtained an estimate of the characteristic radius assuming spherical absorbers of 505 h^{-1} kpc with 95% confidence lower and upper bounds of $345 < R < 1520 \ h^{-1}$ kpc. For the sample of weaker lines with $W_0 > 0.24$ Å, we found the same number of coincidences and 20 anticoincidences, which gave a somewhat smaller radius estimate of 275 h^{-1} kpc and 95% confidence limits of $220 < R < 425 \ h^{-1}$ kpc. Finally, for randomly inclined disklike absorbers, we found the characteristic radii to be $\sim 30\%$–40% larger.

We have also presented a new statistical technique to test the relative likelihood of three geometric models. In particular, we considered spherical absorbers, with and without a distribution in size, as well as pseudo-filamentary and disklike absorbers. We ruled out a single population of spherical absorbers on the basis that spheres with a fixed radius cannot simultaneously produce both the large equivalent width coincidences and anticoincidences observed. The naive model that best reproduces the observed equivalent width distributions was found to be randomly inclined disks with characteristic radius 915 h^{-1} kpc and 95% confidence limits of $560 < R < 1270 \ h^{-1}$ kpc, though filaments and spherical absorbers with a distribution of sizes also reproduce the data well. A qualitative analysis by Charlton et al. (1995) similarly concluded that smooth disklike structures are consistent with existing observations of QSO pairs at $z \simeq 2$. These results are not that surprising in view of recent cosmological simulations in which the Lyα absorption arises in structures of low dimensionality with a range of

scales. Further observations of QSO pairs are required to discriminate between the pseudo-filamentary and disklike geometries, as well as more sophisticated models in which there are two relevant length scales: a length measuring the characteristic distance over which the column density drops by, e.g., a factor of 2 compared to its maximum value, and a length measuring the characteristic distance to the next maximum peak in the column density. The results of the likelihood analysis presented in this paper are preliminary and are meant to demonstrate the viability of the method as a powerful new statistical tool for analyzing the data of QSO pairs.

Several of the Lyα absorption systems used in our likelihood analysis appear to lie in the Lyman limit regime, i.e., with column densities above 10^{17} cm^{-2}. If these systems are indeed LLSs, we should see a decrement in the flux in the GHRS data as well as corresponding Mg II absorption lines, since the Mg II absorbers are thought to arise in the same population of objects as the LLSs (Steidel 1993). Inspection of the flux levels in the FOS and GHRS spectra of both QSOs reveals no evidence for either reduced flux or the characteristic signature of LLSs. (The LLS at $z_{LLS} = 0.3997$ in Q0107−025B, discussed in § 4.4, was not included in either the strong- or weak-line samples). Moreover, we see no evidence for corresponding Mg II systems that would be observable in our MMT data down to an equivalent width of ~ 0.30 Å. Finally, many of the apparent high column density systems have line widths that exceed the instrumental LSF. Therefore, it is more likely that they are blends of narrower components that could be resolved in higher resolution data. Because the line density is so low, the blends cannot be due to just chance superposition, and provides indirect evidence for strong correlations of the Lyα forest lines on velocity scales less than 150 km s^{-1}. Clustering has been detected in the *HST* Key Project catalog of absorbers ($0 < z < 1.3$) on scales of 250–500 km s^{-1} (Ulmer 1996). For clustered absorbers, the sizes of the Lyα absorbers determined from the likelihood analysis in the previous section would be overestimated since the strong lines tend to drive the estimated radius upward.

In order to extend the observations to lower redshifts and therefore smaller transverse dimensions, we have also obtained GHRS data of the pair. We found two common systems with velocity differences less than 150 km s^{-1}. We also observed three Lyα absorption systems in one line of sight and not the other, although a line of the same strength could have been seen. The path length separations at the redshifts of the common systems are about 100 h^{-1} kpc. We need better SNR in the spectrum of Q0107−025A before the GHRS spectra can be used to set limits on the Lyα absorber size in the redshift range $0 < z < 0.23$. Nevertheless, we can place some interesting limits on the linear extent of a LLS observed in the spectrum of Q0107−025B. The LLS is present at $z_{LLS} = 0.3997$ in the spectrum of Q0107−025B but not in A, despite the existence of common Lyα and possibly C IV features. From this, we inferred a firm upper limit on the diameter of the LLS of 250 h^{-1} kpc. Since LLS are associated with higher column density material than the Lyα and C IV systems, we also inferred that lower column density systems are produced at larger impact parameters than systems with higher column densities, in agreement with hydrodynamical simulations and the statistics of the absorbers (Steidel 1993). See, for example, the contour diagrams of neutral hydrogen column density published in Cen et al. (1994) and Miralda-Escudé et al. (1996), which show that the lower column density contours extend out to larger distances than the higher column density contours, contrary to what is expected for uniform clouds pressure-confined by hot halo gas (Cowie et al. 1995).

The characteristic size of the Lyα absorbers derived in this paper are incompatible with those predicted by the pressure-confined model (Sargent et al. 1980; Ikeuchi & Ostriker 1986) and the standard CDM minihalo model (Rees 1986; Miralda-Escudé & Rees 1993), originally proposed to explain the high-redshift Lyα systems. The models envision the clouds to be in hydrostatic equilibrium and predict the typical impact parameter at which a sight line intercepts a column density 10^{14} cm^{-2} to lie in the range 5–50 h^{-1} kpc for typical Doppler widths and reasonable assumptions about the mean intensity of the background radiation field. Furthermore, structures of the size derived in this paper are not expected to be dynamically stable against gravitational collapse or tidal disruption, though such large sizes can be understood if the gas is in the process of collapse or expansion (Weymann et al. 1995).

At low redshift, there is increasing evidence that the Lyα systems are associated with luminous galaxies, though the degree of association remains a contentious issue. Lanzetta et al. (1995) find that Lyα absorption originates in the extended envelopes of luminous galaxies for impact parameters $\lesssim 160$ h^{-1} kpc, with the implication that most if not all Lyα systems are associated with galaxies. In contrast, Morris et al. (1993; see also Mo & Morris 1994) estimate that no more than 20% of the Lyα absorbers are associated with luminous galaxies, and some of the absorbers have been found in voids (Morris et al. 1993; Stocke et al. 1995). The apparent contradiction may be explained by the fact that the Morris et al. and Stocke et al. results are more sensitive to lower column density absorbers, whereas the Lanzetta et al. data sample column densities of $N(H\ I) \gtrsim 10^{14}$ cm^{-2} comparable to the equivalent width threshold of the strong-line sample. If the luminous galaxies are responsible for most or all the high column density systems, their envelopes would have to be uncomfortably large to be consistent with the sizes derived in this paper.

Similar studies of the relationship between Lyα absorbers and individual galaxies have recently been published by Le Brun et al. (1996) and Bowen et al. (1996). Neither study found evidence for a correlation between Lyα equivalent width and impact parameter. In fact, their results are consistent with the Lyα absorbers being distributed in large-scale filaments or sheets, rather than residing in any particular galaxy. In this scenario, the Lyα absorption systems could plausibly arise in the gaseous bridges between galaxies or in tidal debris built up in small groups of galaxies (Morris & van den Bergh 1994). The upper limit on the baryonic density ($\Omega_b \leq 0.036$ h^{-2}; Walker et al. 1991) also places severe constraints on the geometry of the absorbers. Using reasonable estimates of the ionization background, Rauch & Haehnelt (1995) argue that there are not enough baryons to fill a spherical volume of order 0.5 h^{-1} Mpc radius, even if *all* the baryons are contained in the Lyα absorbers. Thus, they suggest that the Lyα absorption must arise in highly flattened structures with transverse extent approximately ten times the thickness of the clouds.

Flattened structures such as filaments, sheets, or pancakes arise naturally in cosmological simulations of a cold

dark matter universe (Cen et al. 1994; Hernquist et al. 1996; Miralda-Escudé et al. 1996). In the simulations, the absorption systems with column densities of $N(H\ I) \simeq 10^{13}$–10^{15} cm^{-2} are produced in a variety of complex structures including filaments of warm gas that trace the dark matter, sheets of shocked gas resembling Zel'dovich pancakes and velocity caustics. The characteristic size of a filament is of order $0.5\ h^{-1}$ Mpc long and 50–100 h^{-1} kpc thick (Miralda-Escudé et al. 1996). Because of the low overdensities of the absorbers, many are still expanding at some fraction of the Hubble flow (Hernquist et al. 1996). Although the simulations have only been evolved to $z = 2$ and are therefore not entirely comparable to our $z < 1$ observations, they are nevertheless remarkably consistent with our results.

Differences between the line-of-sight velocities of the common absorption features provide information about any systematic motions of the absorbing gas over scales equal to the separation of the lines of sight. The velocity difference on scales of a few kpc from paired lines of sight to the gravitationally lensed QSOs Q2345+007A,B (Foltz et al. 1984), UM673A,B (Smette et al. 1992), and most recently HE1104−1805 (Smette et al. 1995) can be ascribed to measurement errors and a reasonable upper bound to Δv is 20 km s^{-1}. In Dinshaw et al. (1994), evidence for a marginally significant velocity difference of 65 km s^{-1} was detected in the physical pair Q1343+2640A,B with separation ~ 40 h^{-1} kpc. The results presented here provide evidence for a statistically significant velocity difference of ~ 100 km s^{-1} over scales of several hundred kpc, and confirm the trend in Δv as a function of line-of-sight separation.

The correlation of rms velocity difference with line-of-sight separation can be understood if the internal motions of the absorbers are systematic over large scales. For example, it is what one would expect for disklike absorbers with a bulk rotational, inflow or outflow velocity component (Charlton et al. 1995). Similarly, it is consistent with pancake-like structures expanding with the Hubble flow (Haehnelt 1996). The velocity difference expected from Hubble expansion in any gravitational clustering model is $\Delta v = H(z)D_\perp \tan \alpha$, where $D_\perp$ is the perpendicular separation of an absorber situated on the two sight lines and α is the angle between the normal to the surface of the absorber and the line of sight. Therefore, for larger line-of-sight separations, we expect systematically larger rms velocity differences of the common pairs. The trend in velocity is similarly observed in the cosmological simulations.

Miralda-Escudé et al. (1996) plotted the median velocity difference of coincident lines as a function of line-of-sight separation. The velocity differences are unobservably small on the scales sampled by gravitationally lensed QSOs, consistent with the results of Smette et al. (1992, 1995). The velocity differences grow for larger line-of-sight separations, similar to the existing observations of QSO pairs. The theoretical results are not directly comparable to the observational results since the simulated data have been analyzed in a different way from the Gaussian profile fitting method used in this paper.

We are currently obtaining further observations of Q0107−025A,B in order to raise the confidence level of many of the weak lines in the FOS data, specifically so that the question of whether the low column density absorption lines share the same properties as those with high column density may be addressed. We are also obtaining data with the G270H grating to extend the spectral coverage of the FOS data out to the Lyα emission lines of the QSOs in order to eliminate existing ambiguities in the line identification. Finally, we are obtaining FOS data of a third bright QSO ($z = 0.728$, $B_J = 18.4$) lying a few arcminutes from Q0107−025A,B. The existence of this QSO offers a unique opportunity to probe distance scales out to 1 Mpc, and to sample two dimensions transverse to the line of sight. These observations, along with those being carried out on other QSOs with still larger separations (e.g., Turnshek et al., in preparation), should yield additional clues as to the distribution and topology of the clouds at low redshifts.

REFERENCES

Aldcroft, T. 1993, Ph.D. thesis, Stanford Univ.
Bahcall, J. N., et al. 1993, ApJS, 87, 1
———. 1996, ApJ, 457, 19
Bechtold, J., Crotts, A. P. S., Duncan, R. C., & Fang, Y. 1994, ApJ, 437, L83
Blackwell, J., et al. 1993, A User's Guide to the GHRS Software, Version 2.1 (Greenbelt: Goddard Space Flight Center)
Bowen, D. V., Blades, J. C., & Pettini, M. 1996, ApJ, 464, 141
Carswell, R. F., Lanzetta, K. M., Parnell, H. C., & Webb, J. K. 1991, ApJ, 371, 36
Cen, R., Miralda-Escudé, J., Ostriker, J. P., & Rauch, M. 1994, ApJ, 437, L9
Charlton, J. C., Churchill, C. W., & Linder, S. M. 1995, ApJ, 452, L81
Chernomordik, V. V., & Ozernoy, L. M. 1993, ApJ, 404, L5
Cowie, L. L., Songaila, A., Kim, T.-S., & Hu, E. M. 1995, AJ, 109, 1522
Cristiani, S., D'Odorico, S., Fontana, A., Giallongo, E., & Savaglio, S. 1995, MNRAS, 273, 1016
Dinshaw, N., Foltz, C. B., Impey, C. D., & Weymann, R. J. 1998, ApJ, in press
Dinshaw, N., Foltz, C. B., Impey, C. D., Weymann, R. J., & Morris, S. L. 1995, Nature, 373, 223 (Paper I)

Dinshaw, N., Impey, C. D., Foltz, C. B., Weymann, R. J., & Chaffee, F. H. 1994, ApJ, 437, L87
Fang, Y., Duncan, R. C., Crotts, A. P. S., & Bechtold, J. 1996, ApJ, 462, 77
Foltz, C. B., Weymann, R. J., Röser, H.-J., & Chaffee, F. H. 1984, ApJ, 281, L1
Gilliland, R. L. 1994, GHRS Instr. Sci. Rep. 063
Haehnelt, M. G. 1996, in Cold Gas at High Redshift, ed. M. N. Bremer (Dordrecht: Kluwer), 109
Hamann, F., Zuo, L., & Tytler, D. 1995, ApJ, 444, L69
Hernquist, L., Katz, N., Weinberg, D. H., & Miralda-Escudé, J. 1996, ApJ, 457, L51
Hu, E. M., Kim, T.-S., Cowie, L. L., Songalia, A., & Rauch, M. 1995, AJ, 110, 1526
Ikeuchi, S., & Ostriker, J. P. 1986, ApJ, 301, 522
Lanzetta, K. M., Bowen, D. V., Tytler, D., & Webb, J. K. 1995, ApJ, 442, 538
Le Brun, V., Bergeron, J., & Boise, P. 1996, A&A, 306, 691
Lindler, D., Bohlin, R., Hartig, G., & Keyes, C. 1993, FOS Instr. Sci. Rep. CAL/FOS-088, available from STScI
Maoz, D., & Rix, H.-W. 1993, ApJ, 416, 425

DINSHAW ET AL.

McGill, C. 1990, MNRAS, 242, 544
Miralda-Escudé, J., Cen, R., Ostriker, J. P., & Rauch, M. 1996, ApJ, 471, 582
Miralda-Escudé, J., & Rees, M. J. 1993, MNRAS, 260, 617
Mo, H. J., & Morris, S. L. 1994, MNRAS, 269, 52
Morris, S. L., & van den Bergh, S. 1994, ApJ, 427, 696
Morris, S. L., Weymann, R. J., Dressler, A., McCarthy, P. J., Smith, B. A., Terrile, R. J., Giovanelli, R., & Irwin, M. 1993, ApJ, 419, 524
Morton, D. C., York, D. G., & Jenkins, E. B. 1988, ApJS, 68, 449
Petitjean, P., Mücket, J. P., & Kates, R. E. 1995, A&A, 295, L9
Rauch, M., Carswell, R. F., Webb, J. K., & Weymann, R. J. 1993, MNRAS, 260, 589
Rauch, M., & Haehnelt, M. G. 1995, MNRAS, 275, L76
Rees, M. J. 1986, MNRAS, 218, 25P
Rix, H.-W., Guhatharkurta, P., Colless, M., & Ing, K. 1996, MNRAS, submitted
Sargent, W. L. W., Young, P., Boksenberg, M., & Tytler, D. 1980, ApJ, 42, 41
Schneider, D. P., et al. 1993, ApJS, 87, 45
Smette, A., Robertson, J. G., Shaver, P. A., Reimers, D., Wisotzki, L., & Köhler, Th. 1995, A&AS, 113, 199

Smette, A., Surdej, J., Shaver, P. A., Foltz, C. B., Chaffee, F. H., Weymann, R. J., Williams, R. E., & Magain, P. 1992, ApJ, 389, 39
Spitzer, L. Jr. 1978, Physical Processes in the Interstellar Medium (New York: Wiley), 52
Steidel, C. C. 1993, in The Environment and Evolution of Galaxies, ed. J. M. Shull & H. A. Thronson, Jr. (Dordrecht: Kluwer), 263
Stocke, J. T., Shull, J. M., Penton, S., Donahue, M., & Carilli, C. 1995, ApJ, 451, 24
Surdej, J., Arp, H., Gosset, E., Kruszewski, A., Robertson, J. G., Shaver, P. A., & Swings, J. P. 1986, A&A, 161, 209
Tytler, D., Fan, X.-M., Burles, S., Cottrell, L., Davis, C., Kirkman, D., & Zuo, L. 1995, in Proc. ESO Workshop on QSO Absorption Lines, ed. G. Meylan (Heidelberg: Springer), 289
Ulmer, A. 1996, ApJ, 473, 110
Walker, T. P., Steigman, G., Schramm, D. N., Olive, K. A., & Kang, H.-S. 1991, ApJ, 376, 51
Weymann, R. J., Rauch, M., Williams, R., Morris, S. L., & Heap, S. 1995, ApJ, 438, 650
Zhang, Y., Anninos, P., & Norman, M. L. 1995, ApJ, 453, L57